Atmospheric Entry Profiles from the Mars Exploration Rovers Spirit and Opportunity

Paul Withers[a,b,*] and Michael D. Smith[c]

[a] Center for Space Physics, Boston University, 725 Commonwealth Avenue, Boston, MA 02215, USA.

[b] Visiting Research Fellow, Planetary and Space Sciences Research Institute, The Open University, Walton Hall, Milton Keynes, MK7 6AA, Great Britain.

[c] NASA Goddard Space Flight Center, Code 693, Greenbelt, MD 20771, USA.

[*] Corresponding author email address: withers@bu.edu

Number of pages: 69

Number of figures: 12

Number of tables: 9

Proposed Running Head:

Spirit and Opportunity Entry Profiles

Editorial Correspondence to:

Paul Withers

Center for Space Physics, Boston University,

725 Commonwealth Avenue, Boston, MA 02215, USA.

Email: withers@bu.edu

Phone: (617) 353 1531

Fax: (617) 353 6463

Received _____; accepted _____

Formatted for submission to Icarus using LaTeX packages natbib, aasms4, and graphicx

ABSTRACT

We report on accelerometer measurements made by Spirit and Opportunity during their entries through the martian atmosphere. Vertical profiles of atmospheric density, pressure, and temperature with sub-km vertical resolution were obtained from above 80 km altitude to below 10 km altitude. Spirit's temperature profile is $\sim$ 10 K warmer than Opportunity's between 20 km and 80 km. Unlike all other martian entry profiles, Spirit's temperature profile does not contain any large amplitude, long wavelength oscillations. A moderate dust storm occurred on Mars shortly before these two atmospheric entries and differences in atmospheric dust loading may account for some of the differences between the two profiles. Both profiles are very consistent with Mars Global Surveyor Thermal Emission Spectrometer (TES) pressure/temperature profiles at pressures less than 30 Pa. The temperature profiles from Spirit and Opportunity are 4 K and 8 K warmer, respectively, than the corresponding TES profiles between 30 and 200 Pa. Some previous workers believe that previous Mars entry profiles were also too warm in this altitude region. The Spirit and Opportunity entry profiles below about 30 km contain a near-inversion and a strong inversion, respectively. A similar inversion was observed by Mars Pathfinder, but such inversions are inconsistent with TES profiles and other observations. These two problems with Mars entry profiles, high-altitude warming and low-altitude inversions, suggest that the characteristics of this measurement technique are not well-understood at present. This has implications for the operational use of real-time entry data to control a spacecraft's atmospheric entry. It is possible that errors in the treatment of spacecraft attitude are responsible for these problems.

Keywords: Mars, Atmosphere; Data Reduction Techniques; Atmospheres, Dynamics [http://icarus.cornell.edu/information/keywords.html]

1. Introduction

We have used data from the entry, descent, and landing (EDL) of the two Mars Exploration Rovers (MERs), Spirit and Opportunity, to obtain two profiles of martian atmospheric density, pressure, and temperature from >80 km to <10 km altitude. These are the first vertical profiles of martian atmospheric structure measured during dusty conditions that have good vertical resolution and good vertical coverage. The atmospheric processes that can be observed in such profiles were discussed by Magalhães et al. (1999), who also compared the advantages and disadvantages of this measurement technique to those of other techniques. The thermal structure of the martian atmosphere is sensitive to radiative forcing from suspended dust and to diabatic heating associated with atmospheric dynamics (Zurek et al., 1992; Leovy, 2001). It is also perturbed by a wide variety of waves and tides (Leovy and Zurek, 1979; Banfield et al., 2000; Withers et al., 2003).

In situ atmospheric entry profiles currently provide our best knowledge of the thermal structure of the atmospheres of Venus, Jupiter, and Titan (Seiff et al., 1980, 1998; Fulchignoni et al., 2002; Fulchignoni, 2005), yet several groups have expressed scepticism about the accuracy of such profiles at Mars (Clancy et al., 2000; Wilson and Richardson, 2000). We compared the MER profiles to near-collocated and near-simultaneous Mars Global Surveyor (MGS) Thermal Emission Spectrometer (TES) profiles of atmospheric pressure and temperature to test whether a systematic bias exists in atmospheric profiles derived from *in situ* entry data.

The MER project sent two nearly-identical rovers to Mars (Garvin et al., 2003; Squyres et al., 2004a,b). The "MER–2" rover, which was launched on the "MER–A" mission to Gusev Crater on 10 June 2003, was later renamed "Spirit". The "MER–1" rover, which was launched on the "MER–B" mission to Meridiani Planum on 7 July 2003, was later renamed "Opportunity". The positions and times of the two landings are shown in Table 1.

[Table 1]

In Section 2 we discuss the MER entry systems, entry measurements, data availability, and the entry states. In Section 3 we discuss the trajectory reconstruction process. In Section 4 we discuss the atmospheric structure reconstruction process. In Section 5 we discuss the spacecraft attitude during entry. In Section 6 we extend the atmospheric structure reconstruction to higher altitudes. In Section 7 we discuss our results. In Section 8 we discuss possible applications of these results. In Section 9 we discuss potential improvements to these results. Since the MER entry measurements were not made by the scientific payload, the archived datasets are not accompanied by extensive documentation, nor have papers been published describing the data processing. Therefore Sections 3–6 are intended to be comprehensive.

2. Atmospheric Entry

2.1. Entry Systems

The design of the MER spacecraft for cruise and EDL was based on the successful Mars Pathfinder design (Spencer et al., 1999; Crisp et al., 2003). Each MER spacecraft consisted of a cruise stage, which was jettisoned at Mars arrival, and an axisymmetric entry capsule. The entry capsule consisted of a 70° sphere-cone ablative front heatshield with Viking-era design heritage and a conic backshell. Inside the entry capsule was a lander. Inside the lander was a rover.

Each MER entry capsule entered the martian atmosphere after its interplanetary cruise at a speed of over 5 km s^{-1} without entering Mars orbit. Aerodynamic drag decelerated the entry capsule as it descended. A parachute was deployed from the rear of the backshell at 5–10 km altitude, when the speed of the entry capsule was a few hundred metres per second.

The front heatshield was jettisoned shortly afterwards and the lander was then lowered beneath the backshell on a 20 m bridle. About one minute after parachute deployment, the lander was at about 100 m altitude and travelling at about 100 m s^{-1}. A cocoon of airbags around the lander then inflated as retrorockets on the backshell fired to decrease both the vertical and horizontal components of the lander velocity. The bridle joining the lander to the backshell and retrorockets was cut at about 10 m altitude when the lander had a speed of about 10 m s^{-1}. The lander fell to the ground and bounced many times, protected by its airbags, as it rolled to a stop. The airbags were later deflated in preparation for the departure of the rover from the now-useless lander.

All these events during EDL were controlled autonomously by the MER computer. The EDL control algorithm required a steady stream of information to make its decisions, specifically measurements of the deceleration of the lander and changes in the attitude of the lander. We have used these measurements to reconstruct the entry trajectory of each MER and the atmospheric structure along each trajectory.

2.2. Entry Measurements

Each MER carried two Litton LN-200S inertial measurement units (IMUs), one mounted on the backshell and one mounted on the rover (Crisp et al., 2003; Kass et al., 2004). The datastream from the backshell IMU (B-IMU) to the MER computer ceased when the bridle was cut prior to impact, whereas the datastream from the rover IMU (R-IMU) continued after impact. Neither IMU was close to the centre of mass or the symmetry axis of the entry capsule. By contrast, atmospheric structure investigations on previous spacecraft were positioned as close to the centre of mass and symmetry axis as possible. Each IMU contained three identical silicon accelerometers and three identical fibre optic gyroscopes. The onboard processing of raw IMU data, which we now describe, has

significant implications for the trajectory reconstruction process.

Each accelerometer measured one component of the acceleration of a test mass with respect to the body of the IMU. Each test mass was held in a fixed position. Each accelerometer had a fixed dynamic range of -40 g to 40 g, where 1 g = 9.80665 m s^{-2}. Each had a resolution of 2.4 mg and noise level of 1.6 mg when sampled at 400 Hz. Each gyroscope measured the angular velocity at a certain point within the IMU and in a certain direction. The dynamic range, resolution, and noise of the angular velocity measurements are not publicly available. We call these six quantities, which were measured at different points within the IMU, "Type 1 data". Type 1 data were sampled at 400 Hz and then transformed into the three dimensional acceleration vector at a reference position within the IMU and in a reference frame defined with respect to the body of the IMU, and into the three dimensional angular velocity vector at that position and in that reference frame. We call this transformed data "Type 2 data." This transformation was performed by the IMU before any data were output to the MER computer. The reference position and reference frame for each IMU are not publicly available. Type 2 data at 400 Hz were sent to the MER computer, which averaged consecutive blocks of 50 measurements to give an effective sampling rate of 8 Hz, thus generating "Type 3 data." Type 3 acceleration data has a resolution of 50 μg and a noise level of 300 μg.

Type 3 acceleration and angular velocity data measured by the B-IMU before parachute deployment were transformed by the MER computer to acceleration and angular velocity at the entry capsule centre of mass and in the entry capsule reference frame. Type 3 R-IMU data were transformed to the same position and frame. These measurements were then subsampled from 8 Hz to a lower sampling rate, which varied during EDL. Accelerations derived from the B-IMU were not processed further, but accelerations derived from the R-IMU were processed into time-integrated accelerations or velocity changes. These should

not be interpreted as actual velocity changes because they do not include *all* accelerations acting on the spacecraft. Angular velocities derived from the B-IMU and R-IMU were processed into quaternions describing the entry capsule attitude with respect to the J2000 reference frame. The initial entry capsule attitude was required for successful completion of this step. We call these accelerations/time-integrated accelerations and quaternions "Type 4 data." The backshell and lander separated along the bridle after parachute deployment. After this separation, Type 4 data from the B-IMU were referenced to the backshell centre of mass and backshell reference frame, but Type 4 data from the R-IMU were referenced to the rover centre of mass and rover reference frame. The positions of these three centres of mass (entry capsule, rover, and backshell) and orientations of these three reference frames are not publicly available.

2.3. Data Availability and Quality

Each MER spacecraft transmitted simple tones directly to Earth during EDL, but these communications did not return any IMU data to Earth. Neither Type 1 nor Type 2 data were returned to Earth. An incomplete set of Type 3 data (8 Hz) was transmitted from each MER to MGS during EDL and later relayed to Earth. An essentially complete set of Type 4 data at 4 Hz was returned to Earth from each MER after its successful landing.

The MER project released to the Planetary Data System (PDS) Type 3 and 4 data from the EDL phase of each MER mission in August 2004 (Kass et al., 2004). The incomplete 8 Hz Type 3 dataset (called HIGHRATE in the PDS archive) is not presently useful because the B-IMU and R-IMU reference positions and reference frames are not publicly available. The essentially complete 4 Hz Type 4 dataset (TRANSFORMED) is useful. The orientation of the entry capsule reference frame used by the Type 4 data is not publicly available, but we assume, based on an inspection of the data, that its z-axis is

the symmetry axis of the entry capsule and that the centre of mass of the entry capsule is located on that axis.

The mean and standard deviations of each of the pre-entry Type 4 B-IMU accelerations are shown in Table 2. The standard deviations, all about 0.003 m s^{-2}, are consistent with the expected noise level (300 μg). The mean pre-entry accelerations are not zero. If these measurements were made accurately and transformed accurately to the centre of mass of the entry capsule, then the mean of each pre-entry acceleration should be zero. Since each Type 4 acceleration measurement is a complicated function of the measurements of three accelerometers and three gyroscopes, the positions and orientations of these six sensors, and the origin and orientation of the entry capsule frame, rather than the output of a single sensor, we cannot attribute the non-zero pre-entry mean to a simple offset in a sensor's zero level. We did not process the Type 4 B-IMU acceleration data to remove the non-zero pre-entry means. The uncertainty in each measurement must be greater than or equal to the measured noise level and the non-zero pre-entry means show that noise is not the only source of error. Based on these factors, we assigned normally-distributed 1-σ uncertainties of 0.01 m s^{-2} to each Type 4 B-IMU acceleration measurement.

[Table 2]

2.4. Entry States

Initial conditions (3-component vector for position, 3-component vector for velocity, and a scalar for time) are required to reconstruct an entry trajectory from measured accelerations. The full entry states for Spirit and Opportunity are not in the PDS archive, nor have they been published elsewhere as a whole. The entry states can be determined from publicly available information, but some effort is required to do so.

Entry is defined to occur when the spacecraft's radial distance from the centre of mass of Mars reaches a specified value, 3522.2 km (Kass et al., 2004). The radial distances to the landing sites are known (Table 1). The latitudes and longitudes at entry are not publicly available, but the landed latitudes and longitudes are (Table 1). The inertial velocities at entry were 5.63 km s^{-1} (Spirit) and 5.70 km s^{-1} (Opportunity) (Desai and Knocke, 2004). The inertial flight path angle at entry was 11.5° (Desai and Knocke, 2004). The inertial flight path azimuths at entry are not publicly available, but the orientations of the landing ellipse, which should be similar, were 75° (Spirit) and 85° (Opportunity) (Golombek et al., 2003). The time intervals between entry, which is not observable in the time series of measured accelerations, and parachute deployment, which is, are 251.0 s (Spirit) and 250.3 s (Opportunity) (Desai and Knocke, 2004). We identified the time of parachute deployment in the time series of Type 4 B-IMU accelerations by a small decrease in a_z shortly before a simultaneous large change in a_x, a_y, and a_z (Spencer et al., 1999).

First, we assumed an entry state. We reconstructed the trajectory using this entry state and the Type 4 B-IMU accelerations and attitude quaternions. The quaternions were used to relate accelerations expressed in the entry capsule reference frame to accelerations in a Mars-fixed frame. We tested how well the resultant trajectory satisfied the constraints above. This process was repeated until we found an entry state whose subsequent trajectory was reasonably consistent with the constraints. This iterative process succeeded for Spirit, but not Opportunity.

Suspecting a problem with the attitude quaternions, we neglected them, assumed that the aerodynamic deceleration parallel to the atmosphere-relative velocity, $\underline{v_{rel}}$, was the root-sum-square of the three orthogonal Type 4 B-IMU acceleration measurements, and repeated the iterative process (Withers et al., 2003). The iterative process was successful for both Spirit and Opportunity, and the entry state for Spirit was about the same as that

obtained using the quaternions. We conclude that the Type 4 attitude quaternions for Opportunity are unreliable, possibly due to an inaccurate initial attitude. In order to treat the two MER spacecraft consistently, we do not use any quaternions in the remainder of this paper. We use only the Type 4 B-IMU acceleration data. Our estimated entry states are shown in Table 3.

[Table 3]

3. Trajectory Reconstruction

3.1. Method

We used the x, y, and z-axis Type 4 B-IMU acceleration data. The sign convention in the PDS archive is such that a_z is negative at peak deceleration. We reversed the sign of a_z for our convenience. Figures 1–2 show time series of a_x, a_y, $a_n = \sqrt{a_x^2 + a_y^2}$, a_z, and a_n/a_z for Spirit and Opportunity. The data in the PDS archive are given as a function of spacecraft clock (SCLK) time. The UTC and SCLK start and stop times that accompany the data in the PDS archive are inconsistent, so we were not able to convert SCLK times to UTC times. All times in this paper are based on SCLK times. a_z is a smooth function of t, time, but the other panels in Figures 1–2 contain high frequency oscillations, which are probably caused by oscillations in the spacecraft attitude. Differences between the two plots of a_n/a_z, which is closely related to the angle of attack, α, the angle between the symmetry axis of the entry capsule and $\underline{v_{rel}}$, suggest that the angles of attack of Spirit and Opportunity behaved differently during their respective EDLs.

[Figure 1] [Figure 2]

We used the spacecraft attitude, the measured accelerations, and a model for the martian gravitational field to determine the total vector acceleration acting on the

spacecraft. This time series of accelerations was then used in the equations of motion to reconstruct the trajectory.

We determined the spacecraft attitude by assuming that $\alpha = 0$ and the measured axial acceleration, a_z, was directed parallel to $\underline{v_{rel}}$. We do not know the direction of a_x or a_y in a Mars-fixed frame, but the effects of these accelerations on the trajectory should average to zero because the entry capsule rotates about its symmetry axis. We neglected a_x and a_y during the trajectory reconstruction. The entry capsule rotated about its symmetry axis at 2 rpm upon separation from the cruise stage and probably continued to do so until parachute deployment. In order to relate velocities in a Mars-fixed frame to $\underline{v_{rel}}$, we assumed that the atmosphere rotated at the same fixed angular rate, $\underline{\Omega}$, as the solid body of Mars (Table 4). Winds are neglected.

[Table 4]

All latitudes and longitudes in this paper are areocentric. Altitude is not referenced to any equipotential surface. Instead, altitude, z, means $r - r_0$, where r is radial distance from the centre of mass of Mars and r_0 is the radial distance to the relevant landing site (Table 1). We used a second degree and order spherical harmonic model of the martian gravitational field:

$$\underline{g} = \underline{\nabla} U \tag{1}$$

$$U = \frac{GM}{r}\left(1 + \left(\frac{R_{ref}}{r}\right)^2 C_{20} P_{20}\left(\cos\theta\right)\right) \tag{2}$$

$$P_{20}\left(x\right) = \sqrt{5}\,\frac{1}{2}\left(3x^2 - 1\right) \tag{3}$$

where $\underline{g}$ is the acceleration due to the gravitational field of Mars in an inertial frame, U is the gravitational potential, GM is the product of the gravitational constant and the mass of Mars, R_{ref} is a reference radius, P_{20} is the normalised associated Legendre function of

degree 2 and order 0, θ is colatitude, and C_{20} is the tesseral normalised spherical harmonic coefficient of degree 2 and order 0 (Tyler et al., 1992; Smith et al., 1993; Tyler et al., 2000). The sign and normalization conventions for U and P_{20} are defined by Equations 1–3. Values of C_{20}, which is related to the oblateness of Mars, GM, and R_{ref} are given in Table 4. The use of higher order models of the gravitational field does not significantly alter the reconstructed trajectory or atmospheric structure (Magalhães et al., 1999). Note that this expression for $\underline{g}$ does not contain any centrifugal terms.

Our reconstructed trajectories cannot be continued beyond the cutting of the bridle, which occured about 10 m above the surface, because we have used accelerations derived from the B-IMU, not the R-IMU. Some portions of the Type 4 dataset have a sampling rate of faster than 4 Hz. We neglected some measurements to ensure a constant 0.25s sampling rate throughout EDL. We also replaced several missing datapoints by linearly interpolating between neighbouring points. Thus we obtained a complete time series of a_x, a_y, and a_z at 4 Hz from entry to bridle cut. The trajectory was reconstructed from entry until bridle cut, but we shall not discuss results after parachute deployment.

The trajectory reconstruction was performed using the procedures described in Withers et al. (2003). We assumed that the centre of mass of Mars was at rest in some inertial frame. We used a simple, first-order numerical integration routine. The two reconstructed trajectories are shown in Figures 3–4. Conditions at parachute deployment are shown in Table 5. Both MER spacecraft travelled 800 km horizontally between entry and parachute deployment.

[Figure 3] [Figure 4] [Table 5]

3.2. Error Analysis

We used a Monte Carlo error analysis to quantify the uncertainties in our derived trajectories and assumed that all uncertainties were normally distributed. We assumed that the uncertainties in the entry states of Spirit and Opportunity were the same as for Pathfinder (Table 3) (Magalhães et al., 1999). We generated n entry altitudes, where $n = 1000$, by selecting values from a normal distribution specified by the relevant mean and standard deviation in Table 3. We generated the remaining components of n complete entry states in a similar manner. We generated n values of a_z at time t by selecting values from a normal distribution specified by the mean and standard deviation shown graphically in Figures 1–2 for that time. Repeating for all times, we generated n complete time series of a_z. We then reconstructed an entry trajectory for each one of these n entry states and time series of a_z using the techniques described above. We calculated standard deviations of the results as functions of time based on this set of n trajectories.

We did not consider uncertainties due to our zero angle of attack assumption, due to truncation of Equation 2 at second order, due to the neglect of winds, due to the assumption that the centre of mass of Mars is at rest in some inertial frame, or due to errors introduced by our chosen numerical techniques.

4. Atmospheric Structure Reconstruction

4.1. Method

Atmospheric density, ρ, is related to the deceleration by the following equation (Magalhães et al., 1999):

$$ma_z = \frac{\rho A v_{rel}^2 C_A}{2} \tag{4}$$

where m is the spacecraft mass, A is the reference area of the spacecraft, and C_A is the axial force coefficient, which is usually on the order of 2. Values of m and A are given in Table 4.

We used the trajectory from Section 3.1, the assumption that $C_A = 2$, and Equation 4 to calculate an initial estimate for the atmospheric density at each point along the entry trajectory. The magnitude of a_z is small at high altitudes due to the low density. The sign of a_z is sometimes negative at high altitudes, which implies unphysical negative densities, due to measurement errors and noise. We began the atmospheric structure reconstructions at a time corresponding to about 120 km altitude, about 10 km below the entry altitude, to minimize this problem. Given this initial density profile, we calculated an initial estimate of the collocated pressure, p, profile assuming hydrostatic equilibrium:

$$\frac{dp}{dr} = \rho \times (g_r + c_r) \tag{5}$$

where g_r, which is negative and a function of position, is the radial component of Equation 1, and c_r is the radial component of $-\underline{\Omega} \times (\underline{\Omega} \times \underline{r})$. This centrifugal term, which is not included in Equation 1, is small and $|c_r/g_r| \sim 4 \times 10^{-3}$. The boundary condition applied at the top of the atmosphere will be discussed later. The ideal gas law leads to an estimate of the collocated temperature, T, profile:

$$\mu p = \rho \frac{R}{N_A} T \tag{6}$$

where μ is the mass of one mole of the martian atmosphere, R is the universal gas constant, and N_A is Avogrado's number (Table 4). We assumed that the mean molecular mass of the martian atmosphere was uniform.

We now have initial estimates of ρ, p, and T at each point along the entry trajectory. The actual values will differ from these initial estimates because C_A is not exactly 2. We improved the initial estimates using the following iterative process.

MER Project engineers estimated the *likely* entry trajectory and atmospheric structure before EDL occurred. They used numerical simulations to determine $C_A(\alpha)$ at a finite number of points along the likely trajectory (Schoenenberger et al., 2005). Interpolation of $C_A(\alpha)$ between these points required v_{rel}, the Mach number, Ma, or the Knudsen number, Kn:

$$Ma = \frac{v_{rel}}{(\gamma p/\rho)^{1/2}} \tag{7}$$

$$Kn = \frac{1}{\sqrt{2}\pi d^2 n_{nd} D} \tag{8}$$

where γ is the ratio of the heat capacity at constant pressure to the heat capacity at constant volume of the martian atmosphere, d is the diameter of an atmospheric molecule, n_{nd}, which satisfies $n_{nd} = N_A\rho/\mu$, is the atmospheric number density, and D, which satisfies $\pi D^2/4 = A$, is the diameter of the entry capsule (Table 4). We assumed that γ was uniform throughout the atmosphere and used values of d and γ for pure CO_2.

The normal force coefficient, C_N, is also relevant. It satisfies:

$$ma_n = \frac{\rho A v_{rel}^2 C_N}{2} \tag{9}$$

Dividing Equation 9 by Equation 4 gives $a_n/a_z = C_N/C_A$. The aerodynamic database

also specifies $C_N(\alpha)$ at the same points along the likely entry trajectory (Schoenenberger et al., 2005). We used the published aerodynamic database and the initial estimate of ρ, p, and T to find $C_A(\alpha)$, $C_N(\alpha)$, and $C_N/C_A(\alpha)$ as functions of time along the reconstructed trajectory. Since C_N is zero when α is zero, C_N/C_A is a linear function of α for sufficiently small values of α. C_N/C_A is a monotonic function of α for all the trajectory points and values of α given in the published aerodynamic database. We determined α at each point along the trajectory by comparing the measured a_n/a_z, which equals C_N/C_A, to the relevant expression for $C_N/C_A(\alpha)$ at each point along the trajectory. We used these values of α to find the corresponding values of both C_N and C_A at each point along the trajectory. This completed the first atmospheric structure iteration.

We returned to Equation 4 and repeated the cycle using our improved estimate for C_A at each point. The estimated profiles of ρ, p, T, Ma, Kn, α, C_A, and C_N all changed slightly. We repeated this iterative process until the greatest change in the reconstructed density from one iteration to the next was below a set threshold, given in Table 4, when we declared that the process had converged. This process should *always* converge on the correct solution because C_A and C_N are *very* weakly dependent on ρ, p, and T.

This iterative process does not give meaningful results if a_n/a_z is inaccurate, which occurs at high altitude as shown in Figures 1 and 2. To minimize this problem, we assumed that $\alpha = 0$ before a time corresponding to about 80 km altitude.

We label quantities on the upper boundary with a subscript "0". The density scale height at the upper boundary, H_0, can be estimated from an exponential fit to the upper 10 km of the density profile. If the atmosphere is isothermal, then $p_0 = \rho_0 g_0 H_0$ and $T_0 = \mu g_0 H_0 / R$. Since the atmosphere is not perfectly isothermal, these estimates of p_0 and T_0 are slightly incorrect. However, due to the exponential dependence of pressure on altitude, the effects of these errors on $p(r)$ and $T(r)$ two or more scale heights below the

upper boundary are very small. This estimate of p_0 supplied the boundary condition in Equation 5.

The results of the atmospheric structure reconstructions are shown in Figures 5–6 and tabulated in Tables 6 and 7 at 12.5s time intervals.

[Figure 5] [Figure 6] [Table 6] [Table 7]

The assumption of a uniform molecular mass, μ, might not be valid at the highest altitudes (Nier and McElroy, 1977; Bougher et al., 1990; Magalhães et al., 1999). Since $T \propto \mu$, readers can easily scale our T results to those that would be obtained using their preferred $\mu(z)$. The ρ and p results are independent of μ.

The atmospheric structure results will only be reliable if the reconstructed trajectories and atmospheric structures are similar to the "likely" trajectory and atmospheric structure assumed by the engineers who generated the aerodynamic database (Schoenenberger et al., 2005). We assume that they are sufficiently similar.

The surface pressure, p_s, can be estimated from:

$$p_s = p_p \exp\left(\left(r_p - r_s\right)/H_p\right) \tag{10}$$

$$H_p = \frac{RT_p}{\mu g_p} \tag{11}$$

where the subscript p indicates values at parachute deployment. The estimated surface pressures are 720 ± 110 Pa for Spirit and 610 ± 110 Pa for Opportunity, which is consistent with the 1.8 km altitude difference between the two landing sites.

4.2. Error Analysis

We used a Monte Carlo error analysis, similar to that of Section 3.2, to quantify the uncertainties in our derived atmospheric structures and assumed that all uncertainties were normally distributed. We slightly modified the atmospheric structure reconstruction technique from Section 4.1, changing the altitude of the upper boundary and using a fixed T_0 instead of a fitted density scale height. As a consequence, the uncertainty envelopes in Figures 5–6 do not extend as high as the entry interface.

We used each of the n trajectories generated in Section 3.2, where $n = 1000$, the nominal aerodynamic properties, and n values of T_0 to generate an set of n atmospheric structure profiles. Since the reconstruction process fails if any of the axial acceleration measurements are negative (what are the aerodynamics of an entry capsule in a fluid of negative density?), we altered the upper boundary from a time corresponding to about 120 km to a time corresponding to about 100 km. The temperature on the upper boundary, T_0, was selected from a distribution with a mean value of T_x, shown in Table 4, and a standard deviation of 50 K. T_x was chosen based on the results from the nominal atmospheric structure reconstruction. The standard deviation was estimated. Each of the n trajectories was assigned a constant value of T_0.

The n profiles of atmospheric properties thus obtained do not reflect the effects of uncertainties in the aerodynamic database. A conservative estimate of the 1-σ uncertainty in the values of C_A in the aerodynamic database is 5% (Magalhães et al., 1999; Desai et al., 2003). Values of C_N will also be uncertain. It is challenging to incorporate these uncertainties into the error analysis. We accounted for these uncertainties by modifying the results of each of our n atmospheric structure reconstructions *after* they had converged. We multiplied each value of C_A in each profile in our set by $1 + x$, where x is a normally distributed random variable with mean 0 and standard deviation 0.05. We did not modify

our results for C_N. α is proportional to C_N/C_A for all possible flow conditions, so we multiplied each value of α in each profile in our set by $1/1+x$. ρ is inversely proportional to C_A, so we multiplied each value of ρ in each profile in our set by $1/1+x$. Kn is inversely proportional to ρ, so we multiplied each value of Kn in each profile in our set by $1+x$. p is related to the height-integrated value of ρ, so we multiplied each value of p in each profile in our set by $1+x$. T is proportional to p/ρ and is quite insensitive to the value of C_A, so we did not modify our results for T (Withers et al., 2003). Ma is proportional to $\sqrt{T}$, so we did not modify our results for Ma.

Due to the statistical nature of this approach, some of the values of a_z in the n time series were negative. If a trajectory had a negative value of a_z below the upper boundary of the atmospheric structure reconstruction, which implies a negative density, then we did not use the results derived from that trajectory in the atmospheric structure error analysis. Only a small fraction of our n trajectories were thus neglected ($< 1\%$ for Spirit, $< 10\%$ for Opportunity), so this does not significantly affect the error analysis. If the altitude of the upper boundary were higher, then significantly more trajectories would be neglected.

We did not consider uncertainties due to our assumption of zero angle of attack at high altitudes, to our assumption of hydrostatic equilibrium, to our assumption of a constant molecular mass, to errors in C_N, m, or A, or to the issues discussed at the end of Section 3.2.

5. Does $\alpha = 0$?

We assumed that $\alpha = 0$ in the trajectory reconstruction, then permitted $\alpha \neq 0$ in the atmospheric structure reconstruction. Was that assumption, which separates the trajectory and atmospheric structure reconstructions, justified? If $\alpha \neq 0$, then the acceleration parallel to $\underline{v_{rel}}$, $a_\parallel$, is $a_z \cos\alpha + a_n \sin\alpha$ and the perpendicular acceleration, $a_\perp$, is $a_n \cos\alpha - a_z \sin\alpha$.

The trajectory reconstruction requires $a_\parallel$ and neglects $a_\perp$, whereas the IMUs measured a_z and a_n. We define ϵ as the ratio of a_z to $a_\parallel$:

$$\epsilon = \frac{a_z}{a_z \cos\alpha + a_n \sin\alpha} \tag{12}$$

For small α, this becomes:

$$\epsilon - 1 = \frac{\alpha^2}{2} - \frac{a_n}{a_z}\alpha \tag{13}$$

Figures 7 and 8 show that the maximum value of $\epsilon - 1$ is 0.015 for Spirit and 0.010 for Opportunity. Figure 18b of Spencer et al. (1999) shows that the maximum value of $\epsilon - 1$ is about 0.004 for Pathfinder. $\epsilon - 1$ is small at high altitudes for both MER spacecraft, but increases at low altitudes. Note that $\epsilon - 1$ is generally positive, implying that $a_\parallel < a_z$. The actual speed of Spirit or Opportunity at a given time during its EDL will be faster than the results of this paper and the actual altitude will be lower because we assumed that $a_\parallel = a_z$ in Section 3.

[Figure 7] [Figure 8]

Does the assumption that $\alpha = 0$ in the trajectory reconstruction have a significant effect on the derived trajectory and atmospheric structure? Suppose an entry vehicle has $\alpha = 0$ ($\cos\alpha = 1$) above 60 km and $\alpha = 5°$ ($\cos\alpha = 1 - 0.004$) between 60 km and 10 km. Since $a_n/a_z\,\alpha \ll \alpha^2/2$ for $\alpha \sim 5°$ and most atmospheric conditions, the effect of $a_n \sin\alpha$ on $a_\parallel$ can be neglected and $a_\parallel$ assumed to equal $a_z \cos\alpha$. The change in $a_\parallel$, 0.4%, seems small, but it can affect v_{rel} significantly. Suppose v_{rel} is 5000 m s^{-1} at 60 km and 500 m s^{-1} at 10 km in the $a_\parallel = a_z$ reconstruction. The velocity change of 4500 m s^{-1} in this reconstruction becomes $(1 - 0.004) \times 4500$ m s^{-1} in the $a_\parallel = a_z \cos\alpha$ reconstruction, which makes v_{rel}

at 10 km 518 m s^{-1} instead of 500 m s^{-1}, an increase of 3.6%. According to Equation 4, density at about 10 km in the $a_{\|} = a_z \cos\alpha$ reconstruction will be 7.2% smaller than in the $a_{\|} = a_z$ reconstruction. Pressures and temperatures will also be affected.

We also considered the specific cases of Spirit and Opportunity. We derived the trajectory and atmospheric structure for both spacecraft using $a_z \cos\alpha + a_n \sin\alpha$ ("new"), instead of a_z ("old"), as $a_{\|}$. We neglected $a_{\perp}$. The "new" reconstruction is not completely self-consistent because it uses $\alpha\,(t)$ from the "old" reconstruction. Nevertheless, it should be sufficient to indicate general trends.

At parachute deployment, Spirit's new altitude was 200 m lower than the old value, its new latitude was 0.006 degrees further north, its new longitude was 0.02 degrees further east, and its new v_{rel} was 13.2 m s^{-1} (3%) faster. The change in v_{rel} is significantly greater than the uncertainty in the original value, 0.9 m s^{-1}. Consequently, the new density at parachute deployment was 6% smaller, the new pressure was 3% smaller, and the new temperature was 8K (4%) hotter. Changes to the trajectory and atmospheric structure above 40 km were negligible. The original uncertainties at parachute deployment were 5% in ρ, 5% in p, and 1K (0.5%) in T.

At parachute deployment, Opportunity's new altitude was 100 m lower than the old value, its new latitude was 0.001 degrees further north, its new longitude was 0.02 degrees further east, and its new v_{rel} was 12.7 m s^{-1} (3%) faster. The change in v_{rel} is significantly greater than the uncertainty in the original value, 0.7 m s^{-1}. Consequently, the new density at parachute deployment was 6% smaller, new pressure was 2% smaller, and new temperature was 8K (4%) hotter. Changes to the trajectory and atmospheric structure above 30 km were negligible. The original uncertainties at parachute deployment were 5% in ρ, 5% in p, and 1K (0.5%) in T.

The rough estimate and the two specific estimates are consistent. They demonstrate

that seemingly small systematic errors in the acceleration in a Mars-fixed frame can drastically affect the reconstructed atmospheric structure. The effects will be most significant at low altitudes because the fractional error in v_{rel} will be greatest there. Corrections for these effects are clearly important, but they will not be attempted in this work because they require detailed coupling between the trajectory and atmospheric structure reconstruction processes that exceeds the present capabilities of our software.

We have shown that the trajectory and atmospheric structure reconstruction processes are extremely sensitive to α — yet Figures 5–6 show that α is uncertain and rapidly varying. A fully self-consistent trajectory and atmospheric structure reconstruction process, with a rigorous error analysis, that includes α will alter the results of both the trajectory and atmospheric structure reconstructions at low altitudes. It will also increase the uncertainties at low altitudes. The uncertainties in the aerodynamic database will be critically important for such a correction.

6. High Altitude Atmospheric Structure

6.1. Method

The atmospheric structure reconstruction in Section 4 determined atmospheric properties every 0.25 s along the reconstructed trajectory between atmospheric entry and parachute deployment. Results at high altitude, though formally obtained, were so uncertain as to be practically useless. Since we have assumed that all uncertainties are normally distributed, we can use averages of data to determine atmospheric properties at high altitudes with reduced uncertainties, but at the cost of reduced vertical resolution.

Neither spacecraft's velocity changed significantly until below 60 km altitude. In this case, according to Equation 4, $\ln(a_z)$ should change linearly with time if ρ changes

exponentially with z.

We used the trajectory from Section 3.1, which has a sampling rate of 4 Hz. We calculated the mean of the logarithm of the first 10 consecutive acceleration measurements made after the time of entry, then used the anti-logarithm of this mean as our averaged acceleration. We also found the mean value of v_{rel} for this block of 10 datapoints. At these high altitudes, the spacecraft's aerodynamics depend only on α and atmospheric density. We assumed that $\alpha = 0$, since a_n/a_z is not known reliably at high altitudes, then iterated as before to determine the atmospheric density that corresponds to each averaged acceleration. We also found the mean altitude and latitude for each block of 10 datapoints. We repeated this for sequential blocks of 10 acceleration measurements. We determined the density scale height for the ith block, H_i, by:

$$-H_i = \frac{z_{i+1} - z_{i-1}}{\ln \rho_{i+1} - \ln \rho_{i-1}} \tag{14}$$

We did not calculate $H_i = 0$ for the first and last blocks. Atmospheric pressures and temperatures were obtained from ρ and H under the assumption of an isothermal atmosphere:

$$T_i = \mu g_i H_i / R \tag{15}$$

$$p_i = \rho_i g_i H_i \tag{16}$$

The isothermal assumption is not strictly accurate, but it makes the relationship between density and other atmospheric properties very simple. The isothermal assumption is reasonable given the relative weakness of the critical assumption that all uncertainties are normally distributed. The derived upper atmospheric properties for each spacecraft are

shown in Tables 8–9. Spirit's results compare reasonably well with those determined in Section 4.1, though Opportunity's do not.

[Table 8] [Table 9]

6.2. Error Analysis

We used a Monte Carlo error analysis, similar to that of Section 3.2, to quantify the uncertainties in our derived high altitude atmospheric structures and assumed that all uncertainties were normally distributed. We obtained n profiles, where $n = 1000$, of high altitude atmospheric properties from each trajectory in the set of n from Section 3.2 as described above, then calculated standard deviations in the atmospheric properties based on the variability within the set. Since some values of a_z in the n time series were negative, corresponding to unphysical negative densities, we screened the data as follows.

We selected a block of 10 consecutive acceleration measurements from a given trajectory, then discarded any negative values. We calculated the mean of the logarithm of the acceleration measurements within this block using only the remaining positive accelerations, then determined the corresponding density. If 3 or more accelerations in the block of 10 were negative, then we did not determine an atmospheric density for that block nor did we determine a density scale height for the blocks immediately before and after that block. We only determined the standard deviation of density for a given 2.5 s block of 10 data points if we had determined densities for that block in 80% or more of the n trajectories. Standard deviations in density scale heights, temperatures, and pressures were also subjected to this 80% threshold.

These results should be used with caution. This approach reduces the uncertainty in the atmospheric structure due to normally-distributed errors, but its results can be biased

by systematic errors. Opportunity's unusual results could be more revealing about such systematic errors than about the martian atmosphere. Nevertheless, these results are useful because they probe the martian upper atmosphere where observations are sparse.

7. Discussion of Results

7.1. General Characteristics

Spirit's temperature profile does not contain any large amplitude, long wavelength oscillations. Small amplitude, short wavelength oscillations occur below ∼25 km, but they are no larger than the error bars. These oscillations are not present in the pressure profile because $p = \int \rho g dr$. These oscillations are present in the temperature profile because $T \propto p/\rho$. Spirit's temperature profile is a relatively smooth quadratic function of altitude above 30 km, but the shape of the temperature profile changes abruptly around 30 km. Opportunity's temperature profile, which is ∼ 20 K colder at 80 km than Spirit's is, has a large amplitude, long wavelength oscillation around 60 km. Small amplitude, short wavelength oscillations occur below about 30 km, similar to those in Spirit's profile. The temperature in Opportunity's profile decreases by 15 K from 12 km to 8 km.

7.2. Dust

The dust loading in the martian atmosphere can increase significantly from its background level within a few days during the onset of a regional/global dust storm. Micron-sized dust particles, which can be lifted 10–20 km by a dust storm, take days to fall one kilometre and the decay time of a large dust storm is on the order of months (Pollack et al., 1979; Murphy et al., 1990; Smith, 2004). The atmosphere can become hotter by ∼ 15 K over a broad vertical range during a large dust storm (Smith et al., 2001). Atmospheric

dynamics are modified and some atmospheric tidal modes, especially the semidiurnal migrating tide, become stronger (Zurek et al., 1992; Bridger and Murphy, 1998). The effects of dust storms extend at least as high as 160 km (Keating et al., 1998). The effects on the atmosphere may have a global extent even if the region of high dust opacity is relatively small.

A large regional dust storm began on Mars in December 2003, which raised significant amounts of dust near the Opportunity landing site. The spatial distribution of dust in the atmosphere on local, regional, and global scales at the time of each entry will affect the thermal structure of the atmosphere. The Spirit and Opportunity entry profiles are the first measured on Mars in the immediate aftermath of a moderate dust storm. They are also the first datasets with sub-scale height vertical resolution to probe the martian middle atmosphere under dusty conditions.

Figure 9 shows infrared dust opacities, τ, measured at the landing sites of both Spirit and Opportunity by the nadir-looking MGS TES instrument in December 2003 and January 2004. The values have been corrected for topographic differences between the two sites. The LST of all measurements was $\sim$ 13.5 hrs. The longitudes of the Spirit measurements are between 170 and 200°E; the longitudes of the Opportunity measurements are between -10 and 20°E. The latitudes of each series of measurements are close to the latitudes of the respective landing sites. This is due to MGS's near-polar orbit, which has a period $\sim$ 2 hours. The 12 ground tracks that cross the equatorial region each day therefore have a longitudinal spacing of about 30°.

[Figure 9]

Values of τ at the landing sites of both Spirit and Opportunity were about 0.2 from 1 December to 10 December. Values of τ at both sites increased slightly over the next few days, then τ at Opportunity's landing site tripled in less than one day, reaching 0.8 on 15

December. It remained extremely high, but variable, until 25 December, when it started to decrease steadily. The rate constant for the exponential decay in τ between 25 December and 8 January was about $(23 \text{ days})^{-1}$. The rate of decay in τ was three times slower than this between 8 January and 31 January.

Meanwhile, τ at Spirit's landing site increased from 0.2 on 1 December to 0.3 around 21 December and remained between 0.30 and 0.35 until around 25 January. Dust opacities at both landing sites were very similar before 14 December. They were also very similar after 19 January, although the dust opacities were 50% greater in late January than in early December. On the day of Spirit's EDL, τ at Spirit's landing site was 0.34 and τ at Opportunity's landing site was 0.42. On the day of Opportunity's EDL, τ at Spirit's landing site was 0.30 and τ at Opportunity's landing site was 0.28. The local and global-scale dust content of the atmosphere was greater for Spirit's EDL than for Opportunity's, which may account for some of the differences between the two profiles, such as the differences in middle atmospheric temperatures and the differences in temperature oscillations.

7.3. Comparison to TES T(p) Profiles

The MGS TES instrument observed temperature as a function of pressure between the surface and 10 Pa near the two landing sites before and after the landings (Smith et al., 2001). We can validate atmospheric profiles derived from accelerometer data against independent observations for the first time since the PAET experiment in the terrestrial atmosphere in 1971 (Seiff et al., 1973). Figures 10–11 compare MER entry profiles and TES profiles. One TES profile was selected from each day as being the closest in latitude, longitude, and LST to the EDL conditions. The 21 TES profiles in each of Figures 10–11 span a period from ten days before to ten days after the day of EDL.

Both entry profiles are very consistent with the TES profiles at between 10 and 30 Pa. The trend of the TES profiles suggests that the entry profiles would be consistent with the TES profiles at even lower pressures if the TES profiles extended further. The gross shape of the Spirit entry profile between 30 and 200 Pa is not similar to the shapes of the corresponding TES profiles, whereas the gross shape of the Opportunity entry profile in this pressure range is quite similar to the shapes of the corresponding TES profiles. The log-pressure-weighted mean difference in temperature between the Spirit entry profile and the TES profile from the day of EDL over the 30–200 Pa pressure range is 4 K. The corresponding value for Opportunity is 8 K. At pressures greater than 200 Pa, the Spirit entry profile contains a near-inversion and the Opportunity entry profile contains a strong inversion. There are no hints of inversions in the TES profiles closest to EDL, although the two earliest TES profiles in Figure 10 have different lapse rates from the subsequent TES profiles. This change in the shape of the TES profiles is probably a temporal effect related to the dust storm, although spatial effects are also possible. There are significant regional variations in topography near the Spirit landing site and the TES profiles in Figure 10 are distributed over about 30° in longitude (Golombek et al., 2003). The TES profiles compared to the Opportunity profile in Figure 11 exhibit much less variability, possibly due either to the flat regional topography at Meridiani compared to Gusev or the less rapid changes in atmospheric dust loading at the time of Opportunity's EDL compared to Spirit's (Golombek et al., 2003).

The vertical resolution of the TES instrument is about one scale height (Conrath et al., 2000). Uncertainties in its derived atmospheric temperatures at these altitudes are ~ 4 K (Smith, 2004). Uncertainties in the Spirit and Opportunity atmospheric temperatures at these altitudes are ~ 1 K (Tables 6–7). However, the angle of attack effects discussed in Section 5 will increase the uncertainties in the entry profiles. Considering the uncertainties in each measurement technique and the poor vertical resolution of TES, the entry $T(p)$

profiles are reasonably consistent with the TES $T(p)$ profiles. Without knowing how the Opportunity profile continues at lower altitudes, it is difficult to say whether the TES instrument would notice such an inversion.

[Figure 10] [Figure 11]

Figure 12 compares temperature-pressure profiles from Viking Lander 1, Viking Lander 2, Mars Pathfinder, Spirit, and Opportunity. Viking Lander 1 landed at 22°N, 312°N on 20 July 1976, when Ls was 96° and LST was 16:13. Viking Lander 2 landed at 48°N, 134°N on 3 September 1976, when Ls was 117° and LST was 09:49. Mars Pathfinder landed at 19°N, 326°N on 4 July 1997, when Ls was 143° and LST was 02:58 (Seiff and Kirk, 1977; Magalhães et al., 1999). Corresponding values for Spirit and Opportunity are shown in Table 1. All profiles, except Spirit's, have large amplitude, long wavelength oscillations around 1 Pa. The Opportunity and Pathfinder profiles are remarkably similar between 2 and 20 Pa. Spirit's profile stands out as being the warmest between 10 and 100 Pa.

[Figure 12]

7.4. Unusual Aspects of Results

There are two aspects of martian entry profiles that are potentially unusual. First, unusual behaviour at low altitudes ($p > 100$ Pa) is seen in the Pathfinder, Spirit, and Opportunity profiles that were derived from accelerometer data. None of these three spacecraft made successful measurements of atmospheric properties after parachute deployment, so these results cannot be verified against direct pressure/temperature measurements. Viking did not derive atmospheric properties from accelerometer data at pressures greater than 100 Pa.

Several authors have discussed whether or not the inversion in the Pathfinder profile

is an accurate measurement of the atmosphere (Magalhães et al., 1999; Haberle et al., 1999; Colaprete et al., 1999; Colaprete and Toon, 2000; Hinson and Wilson, 2004). The Opportunity inversion appears superficially similar to the Pathfinder inversion, but Spirit's is distinctly different. If these features are real, then the high dust content in the atmosphere during Spirit's entry could explain why Spirit's low altitude temperature structure is dissimilar to Pathfinder's and Opportunity's. If these features are not real, then the relatively high angle of attack of Spirit, by comparison to Pathfinder's or Opportunity's, could be responsible for the difference, as discussed in Section 5. Our current understanding of either the thermal structure of the martian atmosphere around $\sim$ 10 km or the characteristics of this measurement technique is poor. In either case, temperatures derived from accelerometer data in the 10 or so kilometres before parachute deployment by Pathfinder, Spirit, and Opportunity deserve further study.

Second, several workers believe, based on comparison with a wide range of models and other observations, that the Viking and Pathfinder profiles appear too warm by $\sim$ 15 K over a vertical range of about 2 scale heights centred on 100 Pa (Clancy et al., 2000; Wilson and Richardson, 2000). Note that the Viking temperature profiles are *not* derived from accelerometer data at pressures greater than 50 Pa (Seiff, 1976; Seiff and Kirk, 1977). The unusual sequence of measurement techniques used by the Viking Landers has not been repeated by any subsequent mission. A similar, but smaller, warming was observed in the comparison between the Spirit and Opportunity entry profiles and TES profiles (Figures 10 and 11) between 30 and 200 Pa.

The first issue, the problem of unusual low altitude temperature inversions, is restricted to Mars Pathfinder, Spirit, and Opportunity. Atmospheric structure profiles determined from accelerometer data before parachute deployment were consistent with those determined from direct measurements immediately after parachute deployment on Pioneer Venus,

Galileo, and Huygens (Seiff et al., 1980, 1998; Fulchignoni et al., 2002; Fulchignoni, 2005).

The second issue, the problem of too-warm temperatures significantly above the altitude of parachute deployment, might be restricted to Viking, Mars Pathfinder, Spirit, and Opportunity — or it might be common to all atmospheric entry profiles. Our understanding of the thermal structures of the atmospheres of Venus, Jupiter, and Titan is sufficiently poor, and corroborating observations sufficiently rare, that spurious 15 K warmings in portions of the Pioneer Venus, Galileo, and Huygens entry profiles might not be detected.

These two problems, low altitude inversions and warmings at higher altitudes, may or may not be connected. If atmospheric properties are being determined incorrectly by entry measurements in some cases, then operationally important properties, such as dynamic pressure, that are determined onboard in real-time during EDL and used to trigger critical events are also being determined incorrectly. Managers and engineers working on future planetary entry vehicles should be concerned about these potential problems with entry data.

Withers (2004) considered various ways to remove the low-lying temperature inversion from the Pathfinder profile, and falsified all his hypotheses, except contamination of the measured accelerations by centrifugal terms. We have not yet been able to determine whether this effect is truly significant. Withers (2004) did not consider the issues discussed in Section 5. If the problems discussed in this Section are indicative of errors in the derived entry profiles, then the most likely causes are either (a) differences between acceleration measured at the accelerometer and acceleration at the centre-of-mass or (b) differences between axial acceleration and acceleration along the atmosphere-relative velocity vector.

8. Applications of Results

Scientists use first principles-based numerical models of the martian atmosphere extensively (e. g., Bougher et al., 1990; Haberle et al., 1999; Forget et al., 1999). Such models extend our understanding of martian atmospheric processes beyond what can be learned from studies of sparse, isolated observations of a handful of atmospheric properties. Global-scale models have often been validated by comparison to atmospheric measurements that either average over a large vertical (e. g., TES) or horizontal (e. g., radio science) distance, but they have rarely been validated against measurements with excellent spatial resolution, such as entry profiles, due to the scarcity of such observations. The vertical resolution of entry profiles is smaller than the spacing of grid points in present global-scale models, so such comparisons are especially useful for evaluating how accurately a model is parameterizing sub-gridscale processes. Mesoscale models for Mars desperately need to be validated against observations with a suitable spatial scale, such as entry profiles (Rafkin and Michaels, 2003; Toigo and Richardson, 2003).

Numerical models of the martian atmosphere, whether empirical or based upon first principles, had a significant effect on the MER missions. They influenced the initial design of the entry vehicle and EDL systems, required the late addition of the DIMES/TIRS imaging/thruster system to the spacecraft, and influenced the site selection process. As a dust storm raged in the weeks before the two landings, predictions of the atmospheric state for each EDL were updated regularly in response to MGS TES and other observations. The changes in the predictions were so significant that changes were made to the onboard software that would control the EDL process. After two successful landings, it would be productive to compare all the atmospheric predictions that were used during the many stages of the MER missions against observations. This comparison would determine which models worked well and which did not, highlighting the strengths and weaknesses of each, so

that obsolete models can be discarded and resources can be directed to where improvements are most urgently needed.

The MER entry profiles can be analysed in conjunction with other datasets. Comparison to measurements of atmospheric properties that are repeated temporally or spatially, such as TES profiles, Mars Express SPICAM profiles, radio science profiles, or ground-based microwave measurements of atmospheric temperature, enables analyses that would not be possible using just one of these datasets. The possible benefits are greater when models are included as well. For example, TES measurements of atmospheric properties on a global scale over an extended period of time could be assimilated into a numerical model, and the model used to predict the atmospheric conditions experienced during the atmospheric entry of Spirit or Opportunity (Montabone et al., 2005). The benefits provided by the data assimilation can be quantified by comparison of these predictions to observations.

The major advantages of entry profiles are their excellent vertical resolution, excellent vertical coverage, and absolute altitude scale. Many remote sensing measurements of atmospheric properties are made at known pressure levels that cannot be converted into accurate heights. A major disadvantage of entry profiles is that they only provide measurements at one place and one time.

9. Potential Improvements to Results

In the past, entry profiles have been processed and analysed by a well-funded team of scientists working closely with the spacecraft engineers and managers (Seiff and Kirk, 1977; Seiff et al., 1980, 1998; Magalhães et al., 1999; Fulchignoni et al., 2002; Fulchignoni, 2005). The entry profiles presented in this paper have not. If additional information is released by

the MER Project, or the PDS datasets recalibrated, then the results in this paper might change. The most likely things that could happen to change these results are: (a) Release of actual entry states with uncertainties; (b) Release of IMU positions and orientations, making 8 Hz accelerations and angular rates useful; (c) Correction of attitude quaternions; and (d) Recalibration of datasets to remove the non-zero pre-entry means. The results in this paper could also be improved to account for the non-zero angle of attack during the trajectory reconstruction (Section 5).

If the attitude quaternions are sufficiently accurate, then it may be possible to estimate horizontal wind speed and direction along the trajectory. If the coupled parachute-backshell-lander aerodynamics are known sufficiently accurately, then it may be possible to determine density, pressure, and temperature along the trajectory after parachute deployment from IMU data.

10. Conclusions

We have presented measurements made by IMUs on Spirit and Opportunity during their descents into the martian atmosphere in January 2004. Relatively unprocessed, raw data (Type 3 data) are not available continuously during entry and, in the absence of additional information, are not currently useful. The archived attitude quaternions (Type 4 data) appear to be unreliable, so we have not used them in this work. We have used acceleration measurements (Type 4 data) to reconstruct the entry trajectories of both spacecraft and to derive profiles of atmospheric density, pressure, and temperature along these trajectories.

These are the first high-resolution measurements of the extended vertical structure of the martian atmosphere made soon after a moderate dust storm. The impact of dust

storms on the middle/upper regions of the martian atmosphere are not well-understood. The two MER temperature profiles show interesting differences in their middle atmospheric temperatures, the presence or absence of large-amplitude, long-wavelength oscillations, and their temperatures below about 20 km. Explanations of these features might require consideration of the local, regional, and global-scale dust loading in the atmosphere, the large-scale dynamics of the atmosphere, and local topography.

The MER entry profiles are consistent with independent TES observations at pressures less than 30 Pa, are 4–8 K warmer than TES observations between 30 and 200 Pa, and have unusual temperature gradients at lower altitudes. Previous workers have suggested that the Viking and Pathfinder entry profiles are also $\sim$ 15 K too warm around 100 Pa. An unusual temperature gradient was also present at low altitudes in the Pathfinder entry profile, although no such feature was observed in the Pioneer Venus, Galileo, or Huygens entry profile. These two problems merit further study and may be related to inadequate knowledge of the angle of attack of the entry vehicles.

Together with other observations, the Spirit and Opportunity entry profiles can be used to test the many scientific and engineering models of the martian atmosphere that were used for spacecraft hardware design, landing site selection, and EDL software design.

This work is completely reproducible. The results presented here and all the software used to generate them are publicly available from http://www.buimaging.com/withers/. Since this personal website is not as stable an archive as the Planetary Data System, interested readers are encouraged to make copies of these resources.

Acknowledgments

We acknowledge the efforts of the MER EDL and Atmospheric Advisory Teams that contributed to two successful landings and the delivery of the IMU datasets to the PDS.

REFERENCES

Allison, M., McEwen, M., 2000. A post-Pathfinder evaluation of areocentric solar coordinates with improved timing recipes for Mars seasonal/diurnal climate studies. Planet. Space Sci. 48, 215–235.

Atkins, P. W., 2002. *Physical chemistry, 6th edition*. W. H. Freeman.

Banfield, D., Conrath, B., Pearl, J. C., Smith, M. D., Christensen, P., 2000. Thermal tides and stationary waves on Mars as revealed by Mars Global Surveyor Thermal Emission Spectrometer. J. Geophys. Res. 105, 9521–9538.

Bougher, S. W., Roble, R. G., Ridley, E. C., Dickinson, R. E., 1990. The Mars thermosphere. II - General circulation with coupled dynamics and composition. J. Geophys. Res. 95, 14811–14827.

Bridger, A. F. C., Murphy, J. R., 1998. Mars' surface pressure tides and their behavior during global dust storms. J. Geophys. Res. 103, 8587–8602.

Clancy, R. T., Sandor, B. J., Wolff, M. J., Christensen, P. R., Smith, M. D., Pearl, J. C., Conrath, B. J., Wilson, R. J., 2000. An intercomparison of ground-based millimeter, MGS TES, and Viking atmospheric temperature measurements: Seasonal and interannual variability of temperatures and dust loading in the global Mars atmosphere. J. Geophys. Res. 105 (E4), 9553–9572.

Colaprete, A., Toon, O. B., 2000. The radiative effects of martian water ice clouds on the local atmospheric temperature profile. Icarus 145, 524–532.

Colaprete, A., Toon, O. B., Magalhães, J. A., 1999. Cloud formation under Mars Pathfinder conditions. J. Geophys. Res. 104 (E4), 9043–9054.

Conrath, B. J., Pearl, J. C., Smith, M. D., Maguire, W. C., Christensen, P. R., Dason, S., Kaelberer, M. S., 2000. Mars Global Surveyor Thermal Emission Spectrometer (TES) observations: Atmospheric temperatures during aerobraking and science phasing. J. Geophys. Res. 105, 9509–9520.

Crisp, J. A., Adler, M., Matijevic, J. R., Squyres, S. W., Arvidson, R. E., Kass, D. M., 2003. Mars Exploration Rover mission. J. Geophys. Res. 108 (E12), 8061, 10.1029/2002JE002038.

Desai, P. N., Knocke, P. C., 2004. Mars Exploration Rover Entry, Descent, and Landing Trajectory Analysis. In: American Institute of Aeronautics and Astronautics paper 2004-5092, 42nd AIAA Aerospace Science Meeting in Reno, Nevada, USA.

Desai, P. N., Schoenenberger, M., Cheatwood, F. M., 2003. Mars Exploration Rover Six-Degree-of-Freedom Entry Trajectory Analysis. Advances in the Astronautical Sciences 116 (3), 2219–2235.

Forget, F., Hourdin, F., Fournier, R., Hourdin, C., Talagrand, O., Collins, M., Lewis, S. R., Read, P. L., Huot, J., 1999. Improved general circulation models of the Martian atmosphere from the surface to above 80 km. J. Geophys. Res. 104, 24155–24176.

Fulchignoni, M., 2005. HASI Nature paper — submitted. Nature.

Fulchignoni, M., Ferri, F., Angrilli, F., Bar-Nun, A., Barucci, M. A., Bianchini, G., Borucki, W., Coradini, M., Coustenis, A., Falkner, P., Flamini, E., Grard, R., Hamelin, M., Harri, A. M., Leppelmeier, G. W., Lopez-Moreno, J. J., McDonnell, J. A. M., McKay, C. P., Neubauer, F. H., Pedersen, A., Picardi, G., Pirronello, V., Rodrigo, R., Schwingenschuh, K., Seiff, A., Svedhem, H., Vanzani, V., Zarnecki, J., 2002. The characterisation of Titan's atmospheric physical properties by the Huygens atmospheric structure instrument (HASI). Space Science Reviews 104, 395–431.

Garvin, J. B., Weitz, C., Figueroa, O., Crisp, J., 2003. Introduction to the special section: Mars Exploration Rover mission and landing sites. Journal of Geophysical Research (Planets) 108 (E12), 10.1029/2003JE002072.

Golombek, M. P., Grant, J. A., Parker, T. J., Kass, D. M., Crisp, J. A., Squyres, S. W., Haldemann, A. F. C., Adler, M., Lee, W. J., Bridges, N. T., Arvidson, R. E., Carr, M. H., Kirk, R. L., Knocke, P. C., Roncoli, R. B., Weitz, C. M., Schofield, J. T., Zurek, R. W., Christensen, P. R., Fergason, R. L., Anderson, F. S., Rice, J. W., 2003. Selection of the Mars Exploration Rover landing sites. Journal of Geophysical Research (Planets) 108 (E12), 10.1029/2003JE002074.

Haberle, R. M., Joshi, M. M., Murphy, J. R., Barnes, J. R., Schofield, J. T., Wilson, G., Lopez-Valverde, M., Hollingsworth, J. L., Bridger, A. F. C., Schaeffer, J., 1999. General circulation model simulations of the Mars Pathfinder atmospheric structure investigation/meteorology data. J. Geophys. Res. 104 (E4), 8957–8974.

Hinson, D. P., Wilson, R. J., 2004. Temperature inversions, thermal tides, and water ice clouds in the Martian tropics. J. Geophys. Res. 109, E01002, 10.1029/2003JE002129.

Kass, D. M., Schofield, J. T., Crisp, J., Bailey, E. S., Konefat, E. H., Lee, W. J., Litty, E. C., Manning, R. M., San Martin, A. M., Willis, R. J., Beebe, R. F., Murphy, J. R., Huber, L. F., 2004. PDS volume MERIMU_0001. In: MER1/MER2-M-IMU-4-EDL-V1.0, NASA Planetary Data System.

Keating, G. M., Bougher, S. W., Zurek, R. W., Tolson, R. H., Cancro, G. J., Noll, S. N., Parker, J. S., Schellenberg, T. J., Shane, R. W., Wilkerson, B. L., Murphy, J. R., Hollingsworth, J. L., Haberle, R. M., Joshi, M., Pearl, J. C., Conrath, B. J., Smith, M. D., Clancy, R. T., Blanchard, R. C., Wilmoth, R. G., Rault, D. F., Martin, T. Z., Lyons, D. T., Esposito, P. B., Johnston, M. D., Whetzel, C. W., Justus, C. G.,

Babicke, J. M., 1998. The Structure of the Upper Atmosphere of Mars: In Situ Accelerometer Measurements from Mars Global Surveyor. Science 279, 1672–1676.

Leovy, C. B., 2001. Weather and climate on Mars. Nature 412, 245–249.

Leovy, C. B., Zurek, R. W., 1979. Thermal tides and Martian dust storms - Direct evidence for coupling. J. Geophys. Res. 84, 2956–2968.

Lodders, K., Fegley, B., 1998. *The planetary scientist's companion*. Oxford University Press.

Magalhães, J. A., Schofield, J. T., Seiff, A., 1999. Results of the Mars Pathfinder atmospheric structure investigation. J. Geophys. Res. 104 (E4), 8943–8956.

Montabone, L., Lewis, S. R., Read, P. L., Withers, P., 2005. The weather on Mars at the time of MERs and Beagle 2 landing. In: European Geosciences Union General Assembly, Abstract EGU05-A-09628, Vienna, Austria, April 2005.

Murphy, J. R., Toon, O. B., Haberle, R. M., Pollack, J. B., 1990. Numerical simulations of the decay of Martian global dust storms. J. Geophys. Res. 95, 14629–14648.

Nier, A. O., McElroy, M. B., 1977. Composition and structure of Mars' upper atmosphere - Results from the neutral mass spectrometers on Viking 1 and 2. J. Geophys. Res. 82, 4341–4349.

Pollack, J. B., Colburn, D. S., Flasar, F. M., Kahn, R., Carlston, C. E., Pidek, D. G., 1979. Properties and effects of dust particles suspended in the Martian atmosphere. J. Geophys. Res. 84, 2929–2945.

Rafkin, S. C. R., Michaels, T. I., 2003. Meteorological predictions for 2003 Mars Exploration Rover high-priority landing sites. Journal of Geophysical Research (Planets) 108 (E12), 10.1029/2002JE002027.

Schoenenberger, M., Cheatwood, F. M., Desai, P. N., 2005. Static Aerodynamics of the Mars Exploration Rover Entry Capsule. In: American Institute of Aeronautics and Astronautics paper 2005-0056, 43rd AIAA Aerospace Science Meeting in Reno, Nevada, USA.

Seiff, A., 1976. The Viking atmosphere structure experiment - Techniques, instruments, and expected accuracies. Space Science Instrumentation 2, 381–423.

Seiff, A., Kirk, D. B., 1977. Structure of the atmosphere of Mars in summer at mid-latitudes. J. Geophys. Res. 82, 4364–4378.

Seiff, A., Kirk, D. B., Knight, T. C. D., Young, R. E., Mihalov, J. D., Young, L. A., Milos, F. S., Schubert, G., Blanchard, R. C., Atkinson, D., 1998. Thermal structure of Jupiter's atmosphere near the edge of a 5-μm hot spot in the north equatorial belt. J. Geophys. Res. 103, 22857–22890.

Seiff, A., Kirk, D. B., Young, R. E., Blanchard, R. C., Findlay, J. T., Kelly, G. M., Sommer, S. C., 1980. Measurements of thermal structure and thermal contrasts in the atmosphere of Venus and related dynamical observations - Results from the four Pioneer Venus probes. J. Geophys. Res. 85 (A13), 7903–7933.

Seiff, A., Reese, D. E., Sommer, S. C., Kirk, D. B., Whiting, E. E., Niemann, H. B., 1973. PAET: An Entry Probe Experiment in the Earth's Atmosphere. Icarus 18, 525–563.

Smith, D., Neumann, G., Arvidson, R. E., Guinness, E. A., Slavney, S., 2003. Mars Global Surveyor Laser Altimeter Mission Experiment Gridded Data Record IEG025_A.TAB. In: MGS-M-MOLA-5-MEGDR-L3-V1.0, NASA Planetary Data System.

Smith, D. E., Lerch, F. J., Nerem, R. S., Zuber, M. T., Patel, G. B., Fricke, S. K., Lemoine, F. G., 1993. An improved gravity model for Mars: Goddard Mars Model 1. J. Geophys. Res. 98, 20871–20889.

Smith, M. D., 2004. Interannual variability in TES atmospheric observations of Mars during 1999-2003. Icarus 167, 148–165.

Smith, M. D., Pearl, J. C., Conrath, B. J., Christensen, P. R., 2001. Thermal Emission Spectrometer results: Mars atmospheric thermal structure and aerosol distribution. J. Geophys. Res. 106, 23929–23945.

Spencer, D. A., Blanchard, R. C., Braun, R. D., W., T. S., 1999. Mars Pathfinder entry, descent, and landing reconstruction. J. Spacecraft and Rockets 36 (3), 357–366.

Squyres, S. W., Arvidson, R. E., Bell, J. F., Brückner, J., Cabrol, N. A., Calvin, W., Carr, M. H., Christensen, P. R., Clark, B. C., Crumpler, L., Des Marais, D. J., d'Uston, C., Economou, T., Farmer, J., Farrand, W., Folkner, W., Golombek, M., Gorevan, S., Grant, J. A., Greeley, R., Grotzinger, J., Haskin, L., Herkenhoff, K. E., Hviid, S., Johnson, J., Klingelhöfer, G., Knoll, A., Landis, G., Lemmon, M., Li, R., Madsen, M. B., Malin, M. C., McLennan, S. M., McSween, H. Y., Ming, D. W., Moersch, J., Morris, R. V., Parker, T., Rice, J. W., Richter, L., Rieder, R., Sims, M., Smith, M., Smith, P., Soderblom, L. A., Sullivan, R., Wänke, H., Wdowiak, T., Wolff, M., Yen, A., 2004a. The Spirit Rover's Athena Science Investigation at Gusev Crater, Mars. Science 305, 794–800.

Squyres, S. W., Arvidson, R. E., Bell, J. F., Brückner, J., Cabrol, N. A., Calvin, W., Carr, M. H., Christensen, P. R., Clark, B. C., Crumpler, L., Des Marais, D. J., d'Uston, C., Economou, T., Farmer, J., Farrand, W., Folkner, W., Golombek, M., Gorevan, S., Grant, J. A., Greeley, R., Grotzinger, J., Haskin, L., Herkenhoff, K. E., Hviid, S., Johnson, J., Klingelhöfer, G., Knoll, A. H., Landis, G., Lemmon, M., Li, R., Madsen, M. B., Malin, M. C., McLennan, S. M., McSween, H. Y., Ming, D. W., Moersch, J., Morris, R. V., Parker, T., Rice, J. W., Richter, L., Rieder, R., Sims, M., Smith, M., Smith, P., Soderblom, L. A., Sullivan, R., Wänke, H., Wdowiak, T., Wolff, M.,

Yen, A., 2004b. The Opportunity Rover's Athena Science Investigation at Meridiani Planum, Mars. Science 306, 1698–1703.

Toigo, A. D., Richardson, M. I., 2003. Meteorology of proposed Mars Exploration Rover landing sites. Journal of Geophysical Research (Planets) 108 (E12), 10.1029/2003JE002064.

Tyler, G. L., Balmino, G., Hinson, D. P., Sjogren, W. L., Smith, D. E., Woo, R., Armstrong, J. W., Flasar, F. M., Simpson, R. A., Priest, P., 2000. PDS volume MORS_1006. In: MGS-M-RSS-5-SDP-V1.0, NASA Planetary Data System.

Tyler, G. L., Balmino, G., Hinson, D. P., Sjogren, W. L., Smith, D. E., Woo, R., Asmar, S. W., Connally, M. J., Hamilton, C. L., Simpson, R. A., 1992. Radio Science Investigations With Mars Observer. J. Geophys. Res. 97, 7759–7779.

Wilson, R. J., Richardson, M. I., 2000. The Martian Atmosphere During the Viking Mission, I: Infrared Measurements of Atmospheric Temperatures Revisited. Icarus 145, 555–579.

Withers, P., 2004. Should we believe atmospheric temperatures measured by entry accelerometers travelling at "slow" near-sonic speeds? In: Proceedings of the Second International Planetary Probe Workshop, held at NASA Ames Research Center, California, August 2004.

Withers, P., Bougher, S. W., Keating, G. M., 2003. The effects of topographically-controlled thermal tides in the martian upper atmosphere as seen by the MGS accelerometer. Icarus 164, 14–32.

Withers, P., Towner, M. C., Hathi, B., C., Z. J., 2003. Analysis of entry accelerometer data: A case study of Mars Pathfinder. Planet. Space Sci. 51, 541–561.

Zurek, R. W., Barnes, J. R., Haberle, R. M., Pollack, J. B., Tillman, J. E., Leovy, C. B., 1992. Dynamics of the atmosphere of Mars. In: Kieffer, H. H., Jakosky, B. M., Snyder, C. W., Matthews, M. S. (Eds.), Mars. University of Arizona Press, pp. 835–933.

Table 1: Locations and Times of MER Landings

	Spirit	Opportunity
Date[a](UTC)	4 January 2004	25 January 2004
Time of first impact[a](UTC hrs)	04:26	04:55
L_s[b](degrees)	327.7	339.1
Latitude[a],[c](°N)	-4.571892	-1.948282
Longitude[a],[c](°E)	175.47848	354.47417
Radial distance[d](km)	3392.3	3394.1
Local Solar Time[b](hrs)	14:16	13:13

[a] Kass et al. (2004)

[b] From Mars24 Sunclock, http://www.giss.nasa.gov/tools/mars24/, based on Allison and McEwen (2000)

[c] Final landed position, not position of first impact

[d] Smith et al. (2003)

Table 2: Characteristics of Pre-Entry Data

	Spirit	Opportunity
$\overline{a_x}$ (10^{-3} m s^{-2})	-1.4	9.6
$\overline{a_y}$ (10^{-3} m s^{-2})	0.7	-2.0
$\overline{a_z}$ (10^{-3} m s^{-2})	3.7	-3.9
$\sqrt{\overline{a_x^2} - \overline{a_x}^2}$ (10^{-3} m s^{-2})	3.0	3.0
$\sqrt{\overline{a_y^2} - \overline{a_y}^2}$ (10^{-3} m s^{-2})	2.9	2.8
$\sqrt{\overline{a_z^2} - \overline{a_z}^2}$ (10^{-3} m s^{-2})	3.2	3.2

Table 3: Estimated Entry States

	Spirit	Opportunity	1-σ Uncertainty
Time - t_{ref} (SCLK seconds)	2085.625	8194.625	0
t_{ref} (SCLK seconds)	126460000.000	128270000.000	0
Radial distance (km)	3522.2	3522.2	1.7
Areocentric latitude (°N)	-17.7	-2.9	0.04
Areocentric longitude (°E)	161.8	340.9	0.01
Speed[a](km s^{-1})	5.63	5.70	7×10^{-4}
Flight path angle[b](degrees)	11.5	11.5	0.02
Azimuth[c](degrees)	79.0	86.5	0.02

[a] Relative to an inertial frame (Spencer et al., 1999; Withers et al., 2003)

[b] Angle below horizontal of velocity vector in inertial frame

[c] Angle east of north of velocity vector in inertial frame

Table 4: Relevant Physical Properties and Constants

GM[(a)](m^3 s^{-2})	4.2828×10^{14}
R_{ref}[(a)](km)	3394.2
C_{20}[(a)]	-8.75981 $\times 10^{-4}$
Ω[(b)](rad s^{-1})	$2\pi/\left(24.6229 \times 60^2\right)$
μ[(c)](kg mol^{-1})	43.49×10^{-3}
d_{CO2}[(d)](m)	4.64×10^{-10}
γ_{CO2}[(e)]	7/5
R[(b)](J K^{-1} mol^{-1})	8.31451
N_A[(b)](mol^{-1})	6.022×10^{23}
A[(d)](m^2)	$\frac{\pi}{4} \times 2.648^2 = 5.507$
m[(f)](kg)	827.0 (Spi.), 832.2 (Opp.)
T_x (K)	160 (Spi.), 160 (Opp.)
Convergence Threshold	10^{-3}

[(a)] Tyler et al. (2000)

[(b)] Lodders and Fegley (1998)

[(c)] Magalhães et al. (1999)

[(d)] Schoenenberger et al. (2005)

[(e)] Ideal linear polyatomic gas (Atkins, 2002)

[(f)] Desai and Knocke (2004)

Table 5: Conditions at Parachute Deployment With 1-σ Uncertainties

	Spirit	Opportunity
Time - t_{ref} (SCLK seconds)	2336.375	8444.625
Altitude (km)	7.5 ± 1.7	6.2 ± 1.8
v_{rel} (m s^{-1})	410.98 ± 0.77	429.68 ± 0.81
Latitude (°N)	-14.528 ± 0.039	-1.957 ± 0.041
Longitude (°E)	175.411 ± 0.013	354.413 ± 0.013

Table 6: Reconstructed Atmospheric Structure With 1-σ Uncertainties: Spirit

$t_{SCLK} - t_{ref}$	z (km)	ρ (kg m^{-3})	p (Pa)	T (K)
2110.625	103.5 ± 1.7	2.79E-07 ± 5.85E-08	6.34E-03 ± 1.93E-03	118.7 ± 52.8
2123.125	91.5 ± 1.7	1.18E-06 ± 8.20E-08	3.33E-02 ± 2.60E-03	147.4 ± 11.7
2135.625	80.4 ± 1.7	4.91E-06 ± 2.70E-07	1.39E-01 ± 7.51E-03	148.4 ± 2.8
2148.125	70.2 ± 1.7	1.80E-05 ± 9.02E-07	5.14E-01 ± 2.60E-02	149.4 ± 1.0
2160.625	60.8 ± 1.7	5.49E-05 ± 2.76E-06	1.63E+00 ± 8.19E-02	155.5 ± 0.8
2173.125	52.5 ± 1.7	1.36E-04 ± 6.93E-06	4.30E+00 ± 2.14E-01	165.6 ± 0.6
2185.625	45.3 ± 1.7	2.88E-04 ± 1.41E-05	9.63E+00 ± 4.88E-01	175.0 ± 0.6
2198.125	39.3 ± 1.7	5.11E-04 ± 2.62E-05	1.80E+01 ± 9.09E-01	184.1 ± 0.6
2210.625	34.5 ± 1.7	7.92E-04 ± 3.94E-05	2.94E+01 ± 1.43E+00	193.8 ± 0.7
2223.125	30.6 ± 1.7	1.10E-03 ± 5.46E-05	4.27E+01 ± 2.17E+00	204.0 ± 0.8
2235.625	27.3 ± 1.7	1.46E-03 ± 7.32E-05	5.79E+01 ± 2.84E+00	206.8 ± 0.8
2248.125	24.5 ± 1.7	1.88E-03 ± 8.80E-05	7.51E+01 ± 3.65E+00	208.4 ± 0.8
2260.625	21.9 ± 1.7	2.38E-03 ± 1.22E-04	9.52E+01 ± 4.75E+00	208.9 ± 0.8
2273.125	19.5 ± 1.7	3.03E-03 ± 1.52E-04	1.19E+02 ± 5.77E+00	205.6 ± 0.9
2285.625	17.1 ± 1.7	3.75E-03 ± 1.85E-04	1.49E+02 ± 7.53E+00	207.1 ± 0.9
2298.125	14.7 ± 1.7	4.68E-03 ± 2.34E-04	1.85E+02 ± 9.52E+00	206.6 ± 0.9
2310.625	12.4 ± 1.7	5.78E-03 ± 2.94E-04	2.30E+02 ± 1.11E+01	207.7 ± 0.9
2323.125	10.0 ± 1.7	7.03E-03 ± 3.53E-04	2.85E+02 ± 1.44E+01	212.3 ± 1.0
2335.625	7.6 ± 1.7	8.57E-03 ± 4.31E-04	3.53E+02 ± 1.74E+01	215.6 ± 1.0

Read 2.79E-07 as 2.79×10^{-7}

Table 7: Reconstructed Atmospheric Structure With 1-σ Uncertainties: Opportunity

$t_{SCLK} - t_{ref}$	z (km)	ρ (kg m^{-3})	p (Pa)	T (K)
8219.625	101.4 ± 1.8	1.71E-07 ± 5.70E-08	7.51E-03 ± 3.77E-03	229.9 ± 140.9
8232.125	89.4 ± 1.8	7.36E-07 ± 6.55E-08	2.30E-02 ± 3.80E-03	163.3 ± 29.4
8244.625	78.2 ± 1.8	4.63E-06 ± 2.45E-07	1.14E-01 ± 6.86E-03	128.8 ± 4.8
8257.125	67.9 ± 1.8	1.66E-05 ± 8.20E-07	4.63E-01 ± 2.44E-02	146.0 ± 1.5
8269.625	58.6 ± 1.8	5.02E-05 ± 2.55E-06	1.45E+00 ± 6.87E-02	150.6 ± 0.7
8282.125	50.3 ± 1.8	1.29E-04 ± 6.74E-06	3.98E+00 ± 1.96E-01	161.3 ± 0.6
8294.625	43.2 ± 1.8	2.81E-04 ± 1.44E-05	9.03E+00 ± 4.57E-01	168.3 ± 0.6
8307.125	37.3 ± 1.8	5.28E-04 ± 2.63E-05	1.75E+01 ± 9.03E-01	173.0 ± 0.7
8319.625	32.6 ± 1.8	8.53E-04 ± 4.23E-05	2.91E+01 ± 1.51E+00	178.5 ± 0.7
8332.125	28.8 ± 1.8	1.16E-03 ± 5.86E-05	4.28E+01 ± 2.14E+00	192.3 ± 0.8
8344.625	25.8 ± 1.8	1.51E-03 ± 7.70E-05	5.78E+01 ± 2.90E+00	199.8 ± 0.8
8357.125	23.0 ± 1.8	2.00E-03 ± 1.06E-04	7.50E+01 ± 3.87E+00	196.4 ± 0.8
8369.625	20.6 ± 1.8	2.44E-03 ± 1.19E-04	9.51E+01 ± 4.79E+00	203.6 ± 0.8
8382.125	18.2 ± 1.8	2.98E-03 ± 1.54E-04	1.19E+02 ± 5.95E+00	208.1 ± 0.9
8394.625	15.9 ± 1.8	3.45E-03 ± 1.77E-04	1.46E+02 ± 7.28E+00	221.6 ± 0.9
8407.125	13.5 ± 1.8	4.23E-03 ± 2.22E-04	1.80E+02 ± 9.23E+00	221.9 ± 1.0
8419.625	11.1 ± 1.8	5.19E-03 ± 2.71E-04	2.21E+02 ± 1.13E+01	222.8 ± 1.0
8432.125	8.7 ± 1.8	6.86E-03 ± 3.37E-04	2.75E+02 ± 1.39E+01	209.4 ± 1.0
8444.625	6.2 ± 1.8	8.39E-03 ± 4.25E-04	3.43E+02 ± 1.75E+01	213.8 ± 1.0

Table 8: High Altitude Atmospheric Structure With 1-σ Uncertainties: Spirit

$t_{SCLK} - t_{ref}$	z (km)	ρ (kg m^{-3})	p (Pa)	T (K)
2106.750	107.4 ± 1.7	1.57E-07 ± 2.36E-08	3.35E-03 ± 1.04E-03	111.6 ± 33.5
2109.250	104.9 ± 1.7	2.36E-07 ± 2.30E-08	5.72E-03 ± 1.30E-03	126.6 ± 27.2
2111.750	102.4 ± 1.7	3.23E-07 ± 2.51E-08	9.10E-03 ± 1.57E-03	147.1 ± 23.1
2114.250	99.9 ± 1.7	4.37E-07 ± 2.87E-08	1.21E-02 ± 1.50E-03	145.1 ± 15.5
2116.750	97.5 ± 1.7	5.99E-07 ± 3.42E-08	1.72E-02 ± 1.79E-03	149.9 ± 12.4
2119.250	95.1 ± 1.7	7.88E-07 ± 4.28E-08	2.42E-02 ± 2.14E-03	160.7 ± 10.9
2121.750	92.8 ± 1.7	1.03E-06 ± 5.81E-08	3.14E-02 ± 2.32E-03	159.3 ± 8.0
2124.250	90.5 ± 1.7	1.35E-06 ± 7.24E-08	3.76E-02 ± 2.50E-03	145.6 ± 5.2
2126.750	88.2 ± 1.7	1.85E-06 ± 9.54E-08	4.66E-02 ± 2.74E-03	132.2 ± 3.4
2129.250	86.0 ± 1.7	2.55E-06 ± 1.28E-07	6.69E-02 ± 3.72E-03	137.4 ± 2.7
2131.750	83.8 ± 1.7	3.36E-06 ± 1.72E-07	1.01E-01 ± 5.44E-03	156.6 ± 2.6
2134.250	81.6 ± 1.7	4.28E-06 ± 2.12E-07	1.29E-01 ± 6.51E-03	157.9 ± 2.1
2136.750	79.5 ± 1.7	5.59E-06 ± 2.78E-07	1.54E-01 ± 7.65E-03	144.0 ± 1.5
2139.250	77.3 ± 1.7	7.41E-06 ± 3.82E-07	2.03E-01 ± 1.06E-02	143.1 ± 1.2
2141.750	75.3 ± 1.7	9.63E-06 ± 4.78E-07	2.72E-01 ± 1.43E-02	147.9 ± 1.1
2144.250	73.2 ± 1.7	1.24E-05 ± 6.37E-07	3.55E-01 ± 1.79E-02	149.6 ± 0.9

Table 9: High Altitude Atmospheric Structure With 1-σ Uncertainties: Opportunity

$t_{SCLK} - t_{ref}$	z (km)	ρ (kg m^{-3})	p (Pa)	T (K)
8213.250	107.9 ± 1.8	1.14E-07 ± 2.09E-08	3.59E-03 ± 1.17E-02	164.6 ± 546.1
8215.750	105.3 ± 1.8	1.48E-07 ± 2.19E-08	6.15E-03 ± 2.36E-02	217.2 ± 955.5
8218.250	102.8 ± 1.8	1.76E-07 ± 2.18E-08	1.00E-02 ± 5.96E-02	298.7 ± 1991.6
8220.750	100.3 ± 1.8	2.02E-07 ± 2.24E-08	1.14E-02 ± 4.75E-02	294.8 ± 1322.3
8223.250	97.8 ± 1.8	2.39E-07 ± 2.29E-08	8.91E-03 ± 2.70E-03	194.6 ± 57.2
8225.750	95.4 ± 1.8	3.21E-07 ± 2.46E-08	8.94E-03 ± 1.56E-03	145.6 ± 23.0
8228.250	93.0 ± 1.8	4.41E-07 ± 2.98E-08	1.18E-02 ± 1.47E-03	139.8 ± 14.7
8230.750	90.6 ± 1.8	6.02E-07 ± 3.47E-08	1.41E-02 ± 1.20E-03	122.2 ± 8.2
8233.250	88.3 ± 1.8	8.97E-07 ± 5.06E-08	1.62E-02 ± 1.09E-03	94.7 ± 3.4
8235.750	86.0 ± 1.8	1.48E-06 ± 7.83E-08	2.77E-02 ± 1.63E-03	97.5 ± 2.7
8238.250	83.8 ± 1.8	2.13E-06 ± 1.12E-07	4.95E-02 ± 2.82E-03	121.8 ± 2.6
8240.750	81.5 ± 1.8	2.93E-06 ± 1.48E-07	7.51E-02 ± 4.20E-03	133.9 ± 2.3
8243.250	79.4 ± 1.8	3.92E-06 ± 2.02E-07	1.06E-01 ± 5.58E-03	141.0 ± 1.9
8245.750	77.2 ± 1.8	5.20E-06 ± 2.56E-07	1.38E-01 ± 7.03E-03	138.7 ± 1.5
8248.250	75.1 ± 1.8	6.95E-06 ± 3.56E-07	1.88E-01 ± 9.52E-03	141.3 ± 1.2
8250.750	73.0 ± 1.8	9.03E-06 ± 4.66E-07	2.61E-01 ± 1.37E-02	151.4 ± 1.2
8253.250	71.0 ± 1.8	1.15E-05 ± 6.00E-07	3.49E-01 ± 1.80E-02	158.4 ± 1.1

Figure Captions

Figure 1: Time series of a_x, a_y, $a_n = \sqrt{a_x^2 + a_y^2}$, a_z, and a_n / a_z for Spirit. 1-σ uncertainties are shown on each panel by the grey envelope. The 1-σ uncertainty of 0.01 m s^{-2} in a_z is also shown as a horizontal line. The data start at the entry interface and end at parachute deployment.

Figure 2: As Figure 1, but for Opportunity.

Figure 3: Spirit's entry trajectory between the entry interface and parachute deployment. 1-σ uncertainties are shown on each panel by the grey envelope.

Figure 4: As Figure 3, but for Opportunity.

Figure 5: Reconstructed atmospheric structure for Spirit between the entry interface and parachute deployment. 1-σ uncertainties are shown on each panel by the grey envelope. Uncertainties were not calculated at the highest altitudes.

Figure 6: As Figure 5, but for Opportunity.

Figure 7: Time series of $\epsilon - 1$ for Spirit between about 80 km and parachute deployment. 1-σ uncertainties are shown on each panel by the grey envelope.

Figure 8: As Figure 7, but for Opportunity.

Figure 9: TES infrared dust opacity during December 2003 and January 2004. Values for Spirit's landing site are shown by diamonds, values for Opportunity's landing site are shown by crosses. The times of the landings of Spirit and Opportunity are marked.

Figure 10: Comparison of entry profile and TES profiles for Spirit. The thick solid line is a 5-point running mean of Spirit's results. The thin solid lines are 21 TES profiles from a $\pm$ 10 sol window centred on the sol of EDL. The TES profile from the sol of EDL lies close to the centre of the cluster of TES profiles. Uncertainties are not shown.

Figure 11: As Figure 10, but for Opportunity.

Figure 12: Entry profiles from Viking Landers 1 and 2, Mars Pathfinder, Spirit, and Opportunity. Viking data are taken from Seiff and Kirk (1977), who tabulated their results at 4 km intervals. Viking pressure and temperature results below 28 km were obtained using a different measurement technique and are not shown here. Squares indicate Viking Lander 1, triangles indicate Viking Lander 2. Pathfinder data (unmarked solid line) are taken from PDS volume MPAM_0001, which has a 4 Hz sampling rate (Magalhães et al., 1999). Spirit (dashed line) and Opportunity (dotted line) data come from the present paper. 5-point running means of the Pathfinder, Spirit, and Opportunity profiles are shown to reduce distracting high frequency oscillations. Uncertainties are not shown.

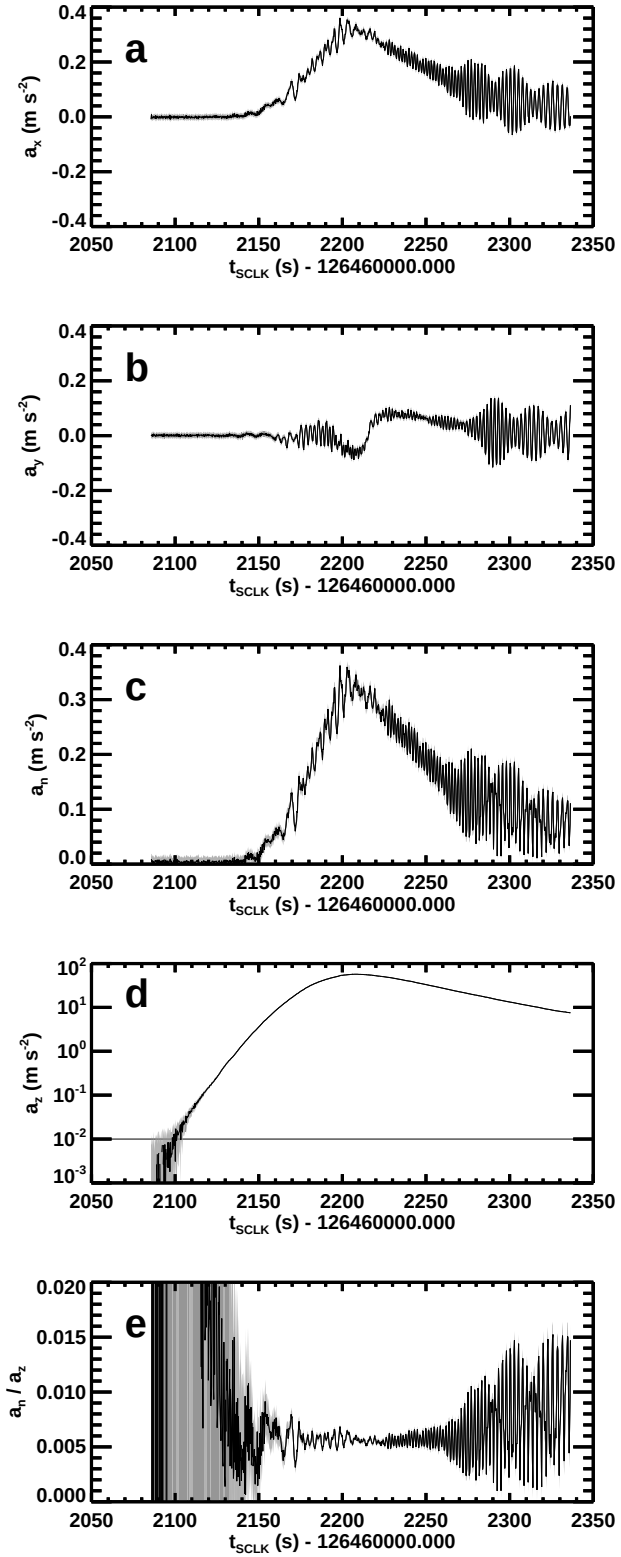

Fig. 1.— Author Paul Withers — Atmospheric Entry Profiles from Spirit and Opportunity

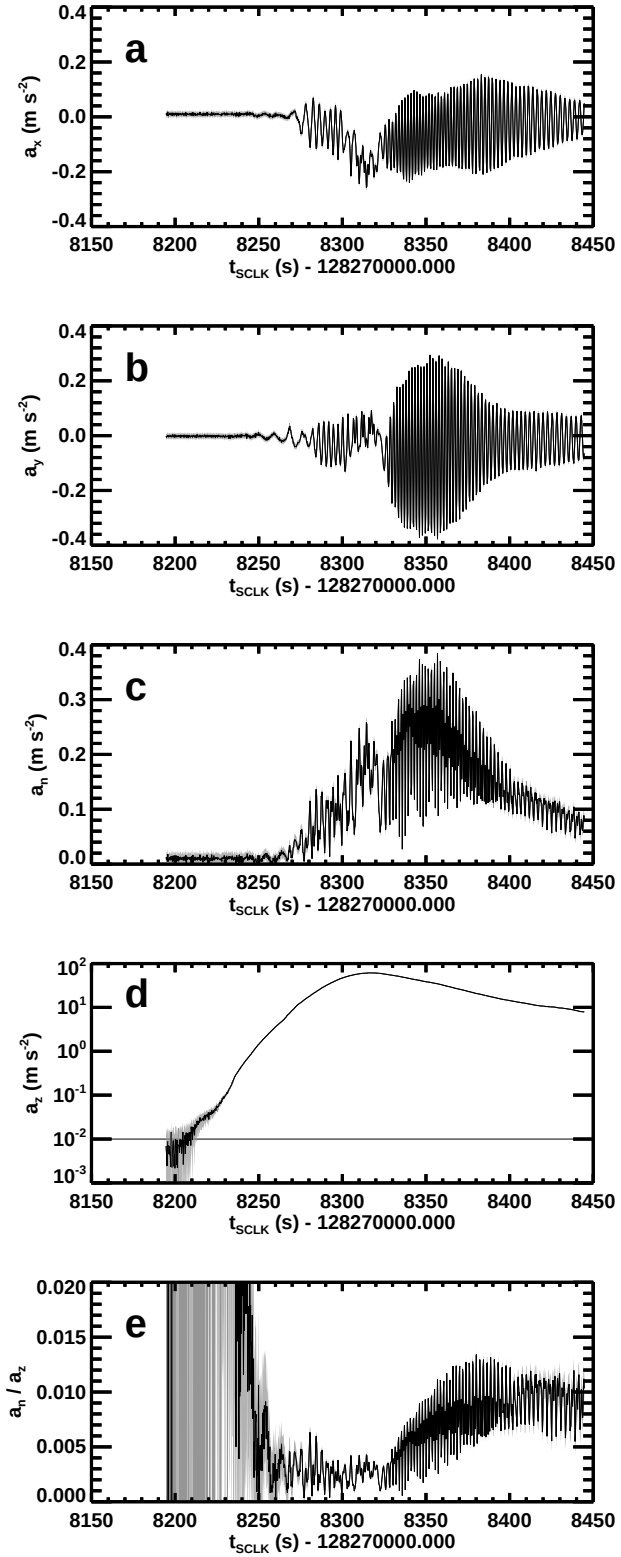

Fig. 2.— Author Paul Withers — Atmospheric Entry Profiles from Spirit and Opportunity

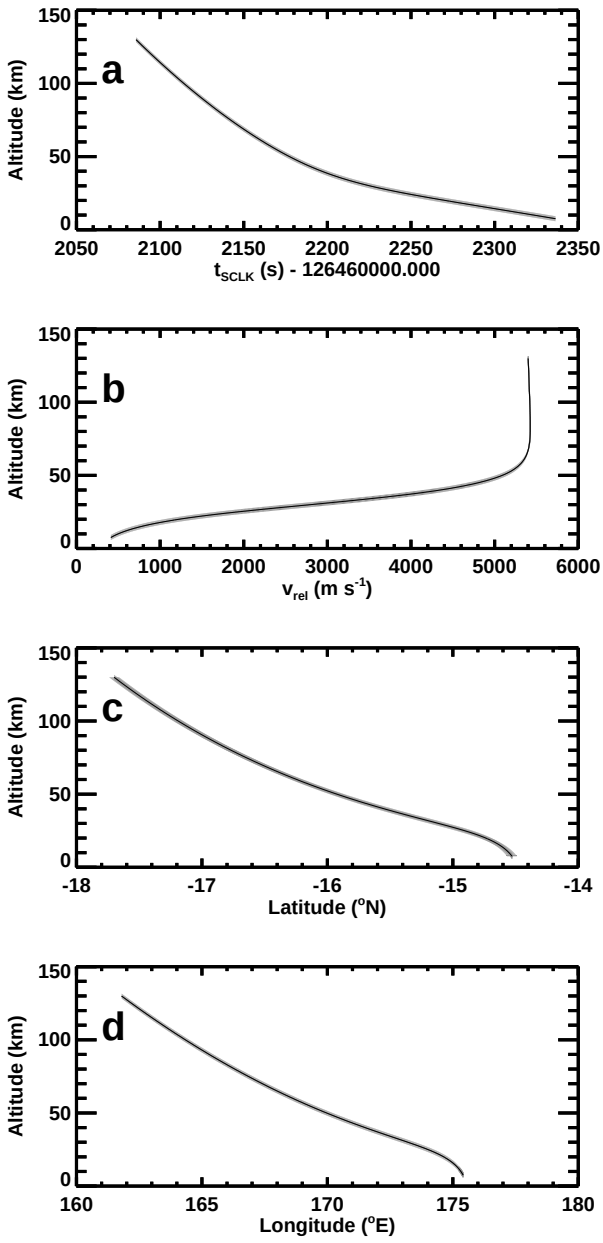

Fig. 3.— Author Paul Withers — Atmospheric Entry Profiles from Spirit and Opportunity

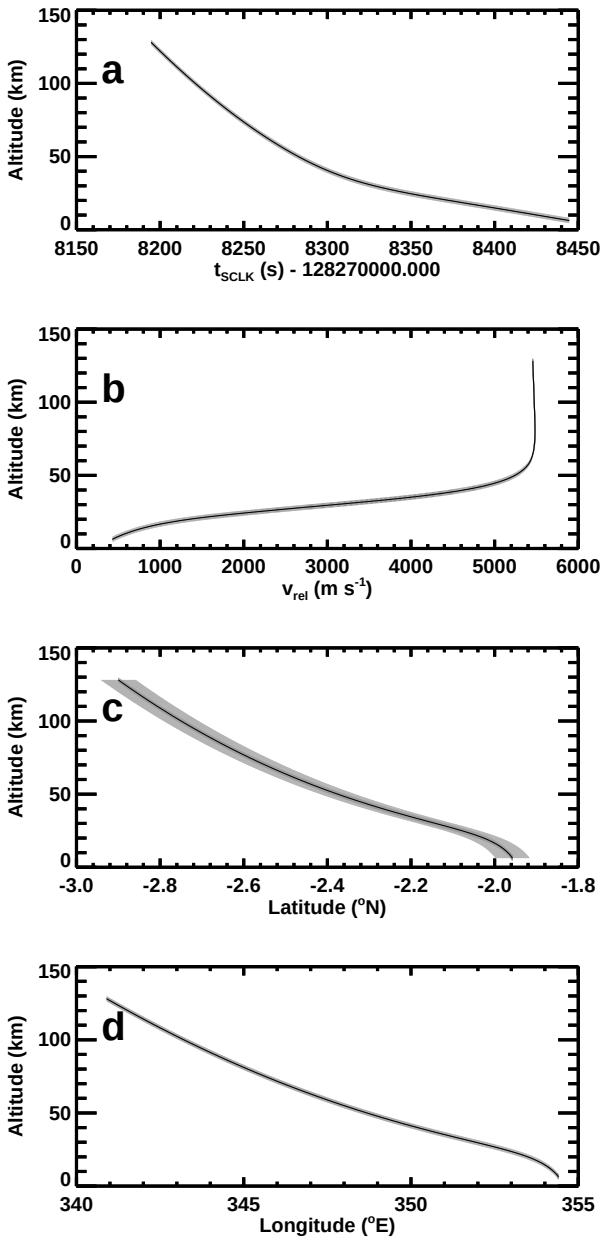

Fig. 4.— Author Paul Withers — Atmospheric Entry Profiles from Spirit and Opportunity

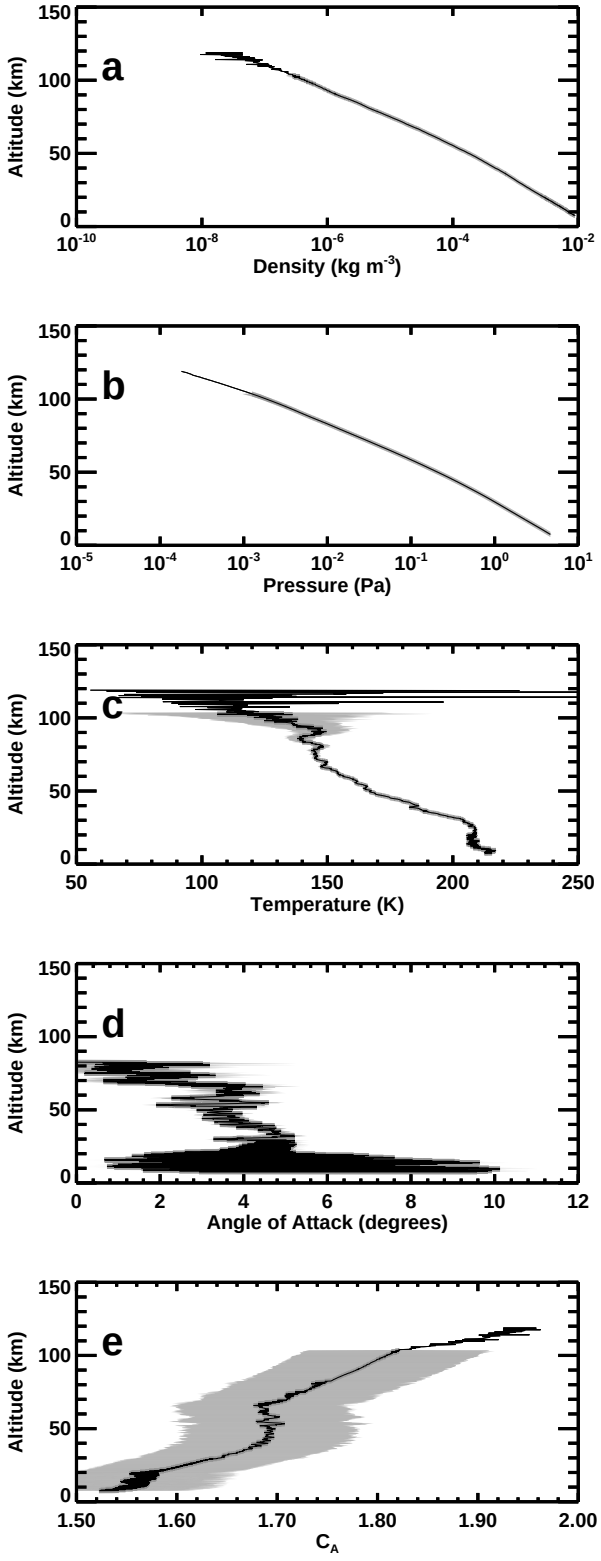

Fig. 5.— Author Paul Withers — Atmospheric Entry Profiles from Spirit and Opportunity

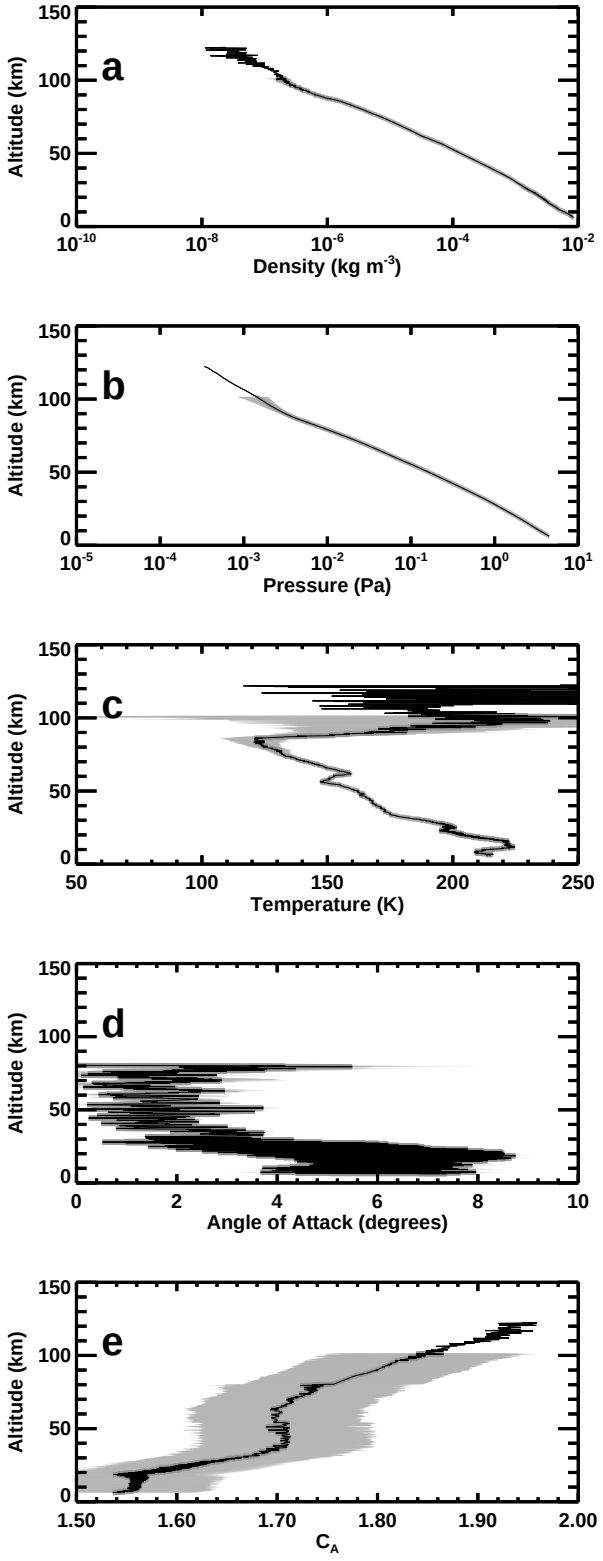

Fig. 6.— Author Paul Withers — Atmospheric Entry Profiles from Spirit and Opportunity

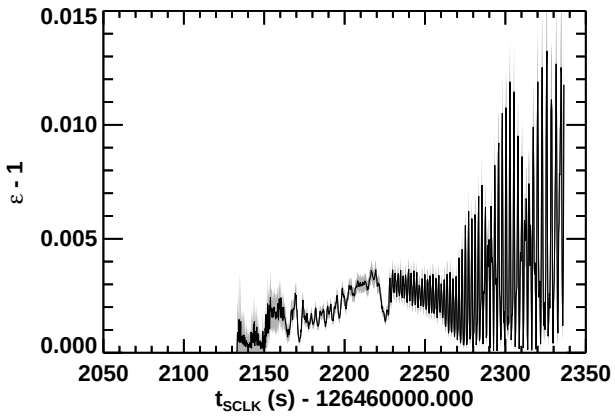

Fig. 7.— Author Paul Withers — Atmospheric Entry Profiles from Spirit and Opportunity

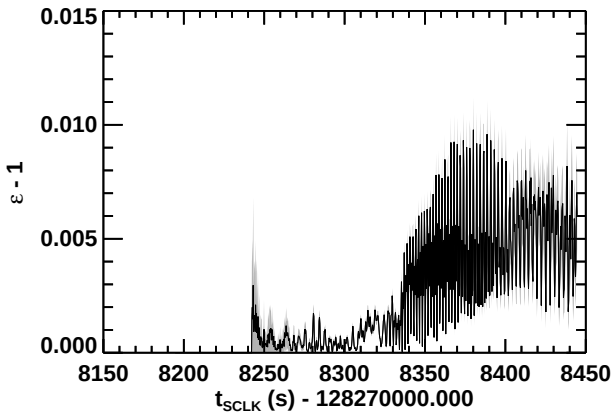

Fig. 8.— Author Paul Withers — Atmospheric Entry Profiles from Spirit and Opportunity

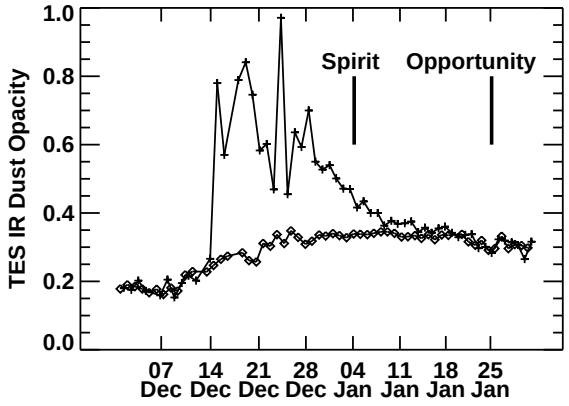

Fig. 9.— Author Paul Withers — Atmospheric Entry Profiles from Spirit and Opportunity

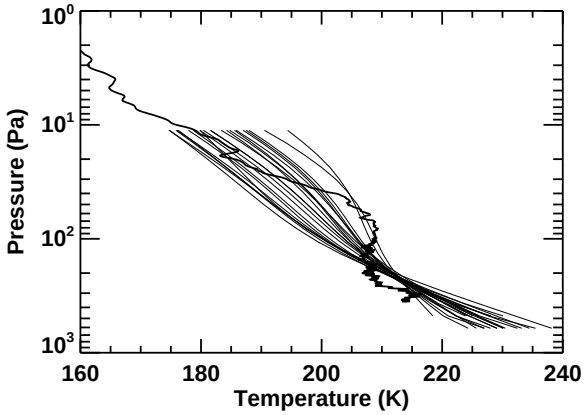

Fig. 10.— Author Paul Withers — Atmospheric Entry Profiles from Spirit and Opportunity

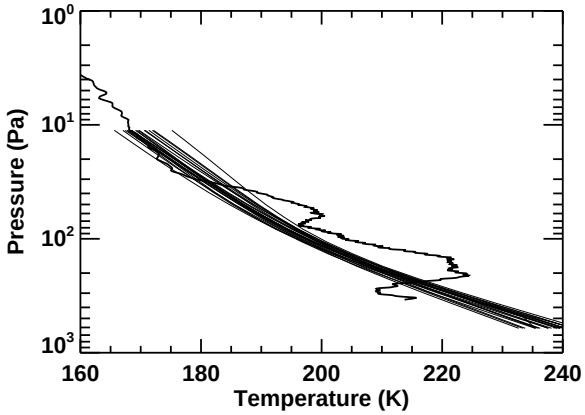

Fig. 11.— Author Paul Withers — Atmospheric Entry Profiles from Spirit and Opportunity

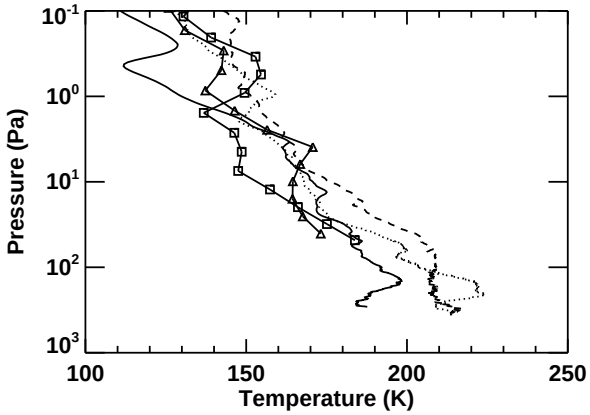

Fig. 12.— Author Paul Withers — Atmospheric Entry Profiles from Spirit and Opportunity